



# TECHNICAL NOTE

D-1008

CALCULATED MODE SHAPES AND PRESSURE DISTRIBUTIONS AT  
FLUTTER FOR A HIGHLY TAPERED HORIZONTAL TAIL  
IN SUBSONIC FLOW

By Gerald L. Hunt and Gerald D. Walberg

Langley Research Center  
Langley Station, Hampton, Va.

NATIONAL AERONAUTICS AND SPACE ADMINISTRATION  
WASHINGTON

April 1962



## NATIONAL AERONAUTICS AND SPACE ADMINISTRATION

## TECHNICAL NOTE D-1008

CALCULATED MODE SHAPES AND PRESSURE DISTRIBUTIONS AT  
FLUTTER FOR A HIGHLY TAPERED HORIZONTAL TAIL  
IN SUBSONIC FLOW

By Gerald L. Hunt and Gerald D. Walberg

## SUMMARY

The mode shapes and pressure distributions of a highly tapered horizontal-tail surface moving in its flutter mode are determined by the subsonic kernel-function method for calculating unsteady aerodynamic loads. The tail surface investigated was previously flutter tested at Mach numbers from 0.75 to 1.20, and a kernel-function flutter analysis was performed for Mach numbers from 0 to 0.98 and reported in NASA TN D-379. The present investigation covers Mach numbers from 0.50 to 0.90 at reduced frequencies determined from the analytical flutter investigation. Those regions of the tail which absorb energy from the air-stream at flutter are identified. The boundaries of these regions do not change appreciably with Mach number in the range investigated; however, a decrease in the aerodynamic stiffness forces with increasing Mach number is indicated.

## INTRODUCTION

The calculation of flutter speeds and frequencies by the solution of eigenvalue problems is a familiar procedure; however, few investigators have proceeded beyond the determination of the eigenvalues to the evaluation of the associated eigenfunctions and hence to the flutter mode and the resulting pressure distribution at flutter. For this reason, little detailed information is available concerning the unsteady pressure distributions and mode shapes existing on lifting surfaces of finite span at flutter. A knowledge of these pressure distributions and mode shapes should facilitate a better understanding of the nature of flutter. Accordingly, flutter mode shapes and pressure distributions calculated for Mach numbers up to 0.90 are presented herein for a horizontal-tail configuration obtained by joining the exposed semispans of the experimental model of reference 1. The configuration investigated thus has a panel (semispan) aspect ratio of 1.66, taper ratio of 0.176, and leading-edge sweep angle of  $30^\circ$ .

Subsonic flutter boundaries for this horizontal-tail surface have been calculated in reference 1 by the kernel-function method of references 2 and 3 and are in good agreement with experiment at Mach numbers below 0.90. This agreement suggests that, for this configuration, theoretical pressure distributions calculated by the method of references 2 and 3 should be similar to the actual pressure distributions existing on the surface at flutter. Therefore, the kernel-function method is also employed in the present analysis. The kernel-function method for calculating unsteady aerodynamic loads is a lifting-surface theory involving direct consideration of the integral equation relating the lift and downwash distributions of oscillating finite wings. Details of this procedure are presented in reference 2.

Since reference 1 is a stability analysis, points of neutral stability (flutter points) were determined, but no explicit presentation of mode shapes or pressure distributions at flutter was made. Flutter pressure distributions and mode shapes are, of course, implicit in the elements of the flutter determinant. The present investigation is thus an extension of reference 1.

In the calculation of the flutter mode shapes, the generalized coordinate ratios at flutter are obtained from simultaneous solution of the equations of motion. The natural vibration modes of the model are combined according to the generalized coordinate ratios to obtain the flutter mode shapes. Modal pressure distributions are similarly combined to yield pressure distributions at flutter. Those regions of the tail which absorb energy from the airstream at flutter are identified.

#### SYMBOLS

$A_{ij}$	generalized aerodynamic force
$A_p$	panel aspect ratio
$b$	streamwise semichord, ft
$b_0$	streamwise semichord at center line, ft
$b_t$	streamwise semichord at tip, ft
$C_{ij}$	complex constants
$C_p(x,y,t)$	coefficient of lifting pressure with phase angle measured from flutter-mode displacement

$C_p^*(x,y,t)$	coefficient of lifting pressure with phase angle measured from first natural-mode component of flutter motion, $\Delta p/q$
$C_{p,0}(x,y)$	amplitude of coefficient of lifting pressure
$f$	frequency, cps
$f_i$	frequency of $i$ th natural vibration mode, cps
$g$	structural damping coefficient
$h(x,y,t)$	instantaneous deflection of point on tail surface in its flutter mode, positive downward, ft
$h_i(x,y)$	normalized, natural mode shape of $i$ th natural vibration mode
$h_j(x,y)$	normalized, natural mode shape of $j$ th natural vibration mode
$h_0(x,y)$	amplitude of surface deflection at flutter, ft
$\dot{h} = \frac{\partial h}{\partial t}$	ft/sec
$I\{ \}$	imaginary part of complex quantity
$i$	unit of imaginaries, $\sqrt{-1}$
$k_0$	reduced frequency, $b_0\omega/V$
$L_j(x,y)$	dimensionless series expression for aerodynamic load distribution due to motion in $j$ th natural vibration mode
$l$	exposed semispan, ft
$M$	Mach number
$m_i$	generalized mass associated with $i$ th natural vibration mode (see eq. (6b)), slugs
$m(x,y)$	local mass per unit area at point $x,y$ (see eq. (6b)), slugs/sq ft
$n$	number of modes

L  
1  
2  
1  
8

$\Delta p(x,y,t)$	distribution of lifting pressure, positive downward, lb/sq ft	
$\Delta p_j(x,y)$	distribution of lifting pressure associated with mode shape $h_j$ (see eq. (2)), $\partial \Delta p / \partial q_j$ , lb/sq ft/ft	
$q$	dynamic pressure, lb/sq ft	
$q_i(t)$	generalized coordinate, $\bar{q}_i e^{i\omega t}$ , ft	
$\bar{q}_i$	complex amplitude of generalized coordinate, ft	L
$q_j(t)$	generalized coordinate, $\bar{q}_j e^{i\omega t}$ , ft	1
$R\{ \}$	real part of complex quantity	2
$S$	area of lifting surface panel, sq ft	1
$t$	time, sec	8
$V$	velocity of airstream, ft/sec	
$x,y,z$	Cartesian coordinates (see fig. 1)	
$\alpha(x,y)$	phase angle between flutter mode and its first natural- mode component (see eq. (10)), positive when flutter mode leads, deg	
$\theta(x,y)$	phase angle between lifting pressure and first natural- mode component of flutter motion (see eq. (13)), positive when pressure leads, deg	
$\Lambda_{le}$	leading-edge sweep angle, deg	
$\lambda$	taper ratio, $b_t/b_0$	
$\mu$	panel mass ratio, ratio of exposed panel mass to mass of truncated cone of air having lower base diameter $2b_0$ , upper base diameter $2b_t$ , height $l$ , and density $\rho$	
$\mu_i$	generalized mass-density ratio for $i$ th natural vibration mode (see eq. (6b))	
$\rho$	density of airstream, slugs/cu ft	

$\phi(x,y)$	phase angle between lifting-pressure coefficient and flutter-mode displacement ( $\theta - \alpha$ ), positive when pressure leads, deg
$\psi$	chordwise coordinate (see fig. 4)
$\omega$	angular frequency, $2\pi f$ , radians/sec
$\omega_i$	angular frequency of $i$ th natural vibration mode
$   $	magnitude of complex quantity
Indices:	
$i, j$	particular natural vibration modes

## DESCRIPTION OF CONFIGURATION

The pressure distributions and mode shapes presented herein were calculated for the tail surface employed in the flutter investigation of reference 1. This model had a panel aspect ratio of 1.66, a taper ratio of 0.176, and a leading-edge sweep angle of  $30^\circ$ . The planform and coordinate system used in the present investigation are presented in figure 1. Model properties are presented in table I. The first three measured natural-vibration modes of the tail surface are presented in reference 1 and are reproduced, for convenience, herein in figure 2.

## ANALYSIS

The present investigation extends the flutter analysis of reference 1 by calculating the mode shapes and oscillatory pressure distributions for the tail surface at flutter. As noted in reference 4, a basic assumption of a Rayleigh-Ritz, or modal, flutter analysis is that the flutter mode may be represented by a superposition of either natural or assumed modal functions in the form

$$h(x,y,t) = \sum_{i=1}^n q_i(t) h_i(x,y) \quad (1)$$

where  $q_i(t) = \bar{q}_i e^{i\omega t}$  is the generalized coordinate of the  $i$ th chosen mode, and  $h_i = h_i(x,y)$  is the corresponding mode shape. (In the

present investigation, the number of modes  $n$  is 3.) Consistent with the Rayleigh-Ritz, or modal, assumption, the pressure distribution  $\Delta p(x,y,t)$  existing on the surface may be regarded as a superposition of pressure modes

$$\Delta p(x,y,t) = \sum_{j=1}^n q_j(t) \Delta p_j(x,y) \quad (2)$$

where  $\Delta p_j(x,y) \equiv \frac{\partial \Delta p}{\partial q_j}$  denotes the distribution of lifting pressure associated with the mode shape  $h_j$ . Hence, the present analysis requires the determination of the values of  $\bar{q}_1$  and  $\Delta p_j$  corresponding to the flutter condition. The normalized, natural mode shapes  $h_1$  are presented in figure 2.

#### Pressure Modes

As noted in reference 1, the equations of motion for the lifting surface at flutter may be written as

$$\left[ 1 - \left( \frac{\omega_1}{\omega} \right)^2 \right] \bar{q}_1 + \frac{1}{k_0^2 \mu_1} (\bar{q}_1 A_{11} + \bar{q}_2 A_{12} + \bar{q}_3 A_{13}) = 0 \quad (i = 1, 2, 3) \quad (3)$$

where

$$A_{ij} = \frac{1}{b_0 l} \iint_S h_i L_j \, dS \quad (4)$$

$$k_0 = \frac{b_0 \omega}{V} \quad (5)$$

$$\frac{1}{\mu_1} = \frac{4\pi \rho l^2 b_0}{M_1} \quad (6a)$$

$$M_1 = \iint_S m(x,y) h_1^2 dS \quad (6b)$$

In equation (4),  $L_j$  is a complex dimensionless expression for the aerodynamic load distribution due to motion in the  $j$ th natural mode and is related to the pressure distribution mode as follows:

$$\Delta p_j(x,y) = 4\pi\rho V^2 \frac{l}{b_0^2} L_j(x,y) \quad (7)$$

The procedure used in evaluating  $L_j$  consists in representing the aerodynamic surface loading by a series expression that automatically satisfies the load conditions at the wing edges. (See ref. 4.) With the load distribution represented in series form, downwash angles at a number of control points on the surface are used as boundary conditions to determine a like number of arbitrary coefficients in the series. This procedure is discussed in references 1, 2, and 3. In the present investigation, nine control points were used. (See fig. 3.) For a given Mach number, mass ratio, and planform,  $L_j$  is a function only of reduced frequency  $k_0$ . In the present investigation, values of  $k_0$  at flutter were taken from the flutter analysis reported in reference 1. These values of  $k_0$  were then substituted into the flutter determinant of reference 1 and the determinant was solved to insure that these reduced frequencies corresponded to flutter conditions (defined as  $g = 0$ ). These values of  $k_0$  were then used to calculate  $L_j$  ( $j = 1, 2, 3$ ) at flutter.

#### Generalized Coordinates

Generalized coordinate ratios at flutter were determined from the simultaneous equations (3). With the previously calculated values of  $L_j$ , the generalized aerodynamic forces  $A_{1j}$  were calculated as described in reference 1. At each Mach number the previously mentioned solution of the flutter determinant provided values of  $\omega_1/\omega$  for a mass ratio  $\mu$  of 60. Substitution of these quantities into equations (3) yields a set of linear, homogeneous, algebraic equations with the values of  $\bar{q}_1$  unknown; that is,

$$\left. \begin{aligned} c_{11}\bar{q}_1 + c_{12}\bar{q}_2 + c_{13}\bar{q}_3 &= 0 \\ c_{21}\bar{q}_1 + c_{22}\bar{q}_2 + c_{23}\bar{q}_3 &= 0 \\ c_{31}\bar{q}_1 + c_{32}\bar{q}_2 + c_{33}\bar{q}_3 &= 0 \end{aligned} \right\} \quad (8)$$

where the values of  $c_{ij}$  are complex constants. Since the coefficient determinant of equations (8) is equal to zero, the equations cannot be solved explicitly for  $\bar{q}_1$ ,  $\bar{q}_2$ , and  $\bar{q}_3$ . The equations can, however, be solved for the ratios  $\bar{q}_2/\bar{q}_1$  and  $\bar{q}_3/\bar{q}_1$ .

#### Mode Shapes and Pressure-Coefficient

##### Distributions at Flutter

The flutter mode shape may be determined from equation (1) which may be written, for three modes, as

$$h(x,y,t) = \left( h_1 + \frac{\bar{q}_2}{\bar{q}_1} h_2 + \frac{\bar{q}_3}{\bar{q}_1} h_3 \right) \bar{q}_1 e^{i\omega t} \quad (9)$$

With  $\bar{q}_1$  chosen equal to unity as a convenient reference for the amplitudes and phase angles of the displacements, there results

$$\begin{aligned} h(x,y,t) &= \left| h_1 + \bar{q}_2 h_2 + \bar{q}_3 h_3 \right| e^{i(\omega t + \alpha)} \\ &= h_0(x,y) e^{i(\omega t + \alpha)} \end{aligned} \quad (10)$$

where  $h_0$  is the displacement amplitude at flutter and  $\alpha = \alpha(x,y)$  is the phase angle between the flutter mode and its first natural-mode component. The natural mode shapes  $h_1$  (fig. 2) were taken from reference 1, and the complex ratios  $\bar{q}_2/\bar{q}_1$  and  $\bar{q}_3/\bar{q}_1$  were obtained from solutions of equations (8).

Distributions of the lifting-pressure coefficient at flutter were obtained by employing equations (2) and (7) as

$$\Delta p(x, y, t) = 4\pi\rho \frac{v^2 l}{b_0^2} (q_1 L_1 + q_2 L_2 + q_3 L_3) \quad (11)$$

Therefore,

$$\begin{aligned} C_p^*(x, y, t) &= \frac{\Delta p(x, y, t)}{\frac{1}{2} \rho v^2} \\ &= \frac{8\pi l}{b_0^2} \left( L_1 + \frac{\bar{q}_2}{\bar{q}_1} L_2 + \frac{\bar{q}_3}{\bar{q}_1} L_3 \right) \bar{q}_1 e^{i\omega t} \end{aligned} \quad (12)$$

Again, choosing  $\bar{q}_1$  equal to unity yields

$$\begin{aligned} C_p^* &= \frac{8\pi l}{b_0^2} |L_1 + \bar{q}_2 L_2 + \bar{q}_3 L_3| e^{i(\omega t + \theta)} \\ &= C_{p,0}(x, y) e^{i(\omega t + \theta)} \end{aligned} \quad (13)$$

where  $\theta = \theta(x, y)$  is the phase angle between the lifting pressure and the first natural-mode component of the flutter motion, and  $C_{p,0}(x, y)$  is the amplitude of the complex lifting-pressure coefficient at flutter.

In considering the distributions of lifting-pressure coefficient at flutter, one must utilize the phase angle between the lifting pressure and the flutter motion. This angle is given by

$$\phi = \theta - \alpha$$

Hence, the lifting-pressure coefficient referenced to the flutter mode may be written as

$$C_p = C_{p,0}(x, y) e^{i(\omega t + \phi)} = C_p^*(x, y, t) e^{-i\alpha} \quad (14)$$

It should be noted that this expression for the lifting-pressure coefficient is a complex number with its real component in phase and its imaginary component  $90^\circ$  out of phase with the displacement at the flutter condition.

## Extraction of Energy From Airstream

It is well known that only the component of the lifting pressure that is in phase with the oscillatory velocity of the lifting surface (i.e., out of phase with the displacement) can contribute to an energy exchange between the surface and the airstream. Thus, if energy is extracted from the airstream, this pressure component must have the same sense as the velocity; that is, the phase angle  $\phi$  must be in the range  $0 < \phi < 180^\circ$ . Thus, energy is extracted from the airstream when the lifting pressure leads the displacement.

## RESULTS AND DISCUSSION

The equations of motion (eqs. (8)) for an oscillating lifting surface were solved for the generalized coordinate ratios of a horizontal tail moving in its flutter mode at Mach numbers from 0.50 to 0.90 for a mass ratio of 60. These generalized coordinate ratios were then used to determine the mode shapes (see eq. (10)) and the lifting-pressure-coefficient distributions (see eq. (14)) existing on the surface at flutter. Those regions of the tail which extract energy from the airstream were identified.

### Flutter-Mode Shapes

Figure 5 presents the maximum amplitude  $h_0(x,y)$  of the flutter-mode shapes as calculated from equation (10). It should be noted that in equation (10),  $h_0$  was referred to a unit displacement of the first natural mode; that is,  $\bar{q}_1 = 1.0$ . Since the calculated flutter mode consists of a complex combination of the natural vibration modes, differences in phase exist between various points on the surface. Contours of the phase angle  $\alpha = \alpha(x,y)$  between the displacement at flutter and its first natural-mode component are presented in figure 6. Reference 1 presents calculated and experimental flutter-frequency ratios which decrease as Mach number increases from 0.50 to 0.90. It may be concluded from this variation of flutter-frequency ratio that the contributions to the flutter mode of the higher natural modes decrease with increasing Mach number. Examination of the flutter-mode amplitudes presented in figure 5 indicates that the contribution to the flutter mode of the third natural mode decreases as Mach number increases. Hence, the flutter modes of the present investigation confirm the conclusion drawn from the flutter-frequency ratios of reference 1. The phase-angle contours of figure 6 show that, as Mach number increases, the phase-angle distributions are roughly similar over the inboard two-thirds of the surface, but decrease in magnitude over the outboard

L  
1  
2  
1  
8

one-third of the surface. These contours also show that the inboard region of the tail leads the first mode component, that the 70-percent-semispan region is nearly in phase with the first mode, and that the tip region lags the first mode, each in varying degrees according to Mach number.

### Pressure Distribution at Flutter

Figure 7 presents distributions of the real and imaginary parts of the complex amplitudes  $R\{C_{p,0}e^{i\phi}\}$  and  $I\{C_{p,0}e^{i\phi}\}$  of the lifting-pressure coefficient referred to the flutter displacement. (See eq. (13).) Since the real part of the lifting-pressure coefficient is in phase with the flutter displacement, it contributes an aerodynamic stiffness force to the tail which may be positive or negative according to its sign. The imaginary part of the lifting-pressure coefficient is  $90^\circ$  out of phase with the flutter displacement, and hence constitutes an aerodynamic damping force.

From the real-component plots of figure 7, it is seen that the chordwise distributions are similar to steady-state pressure-coefficient distributions. It is also seen that while the real-component distributions display the same trend throughout the Mach number range investigated, the magnitudes of the real components decrease with increasing Mach number, particularly near the leading edge. This decrease in the magnitudes of the negative real components may be interpreted as a decrease in the aerodynamic stiffness contribution, which, in turn, would be expected to produce a reduction in flutter frequency with increasing Mach number. The data of reference 1 confirm this expectation by showing a continual decrease in flutter frequency as Mach number increases from 0.50 to 0.90.

From the imaginary-component plots of figure 7, it is seen that while the magnitudes of the pressures decrease with increasing Mach number, the regions of positive and negative out-of-phase pressures retain essentially their same size and location. Hence, in spite of the previously mentioned change in flutter mode with increasing Mach number, the regions of the tail which experience negative aerodynamic damping forces are virtually unchanged from values of  $M = 0.50$  to  $M = 0.90$ .

### Extraction of Energy From Airstream

As indicated in the section "Analysis," those regions of the surface which extract energy from the airstream may be identified by the phase angle  $\phi$  between the lifting pressure and the flutter mode

displacement. Specifically, values of  $\phi$  in the range  $0 < \phi < 180^\circ$  indicate extraction of energy from the stream. Contour plots of  $\phi$  are presented in figure 8. It should be noted that figures 7 and 8 are related, since regions of  $0 < \phi < 180^\circ$  correspond to regions of positive imaginary components of the pressure. Examination of the phase-angle plots of figure 8 shows, as does figure 7, that the boundaries of the unstable regions of the tail are essentially unaffected by Mach number in the range  $0.50 \leq M \leq 0.90$ .

### CONCLUSIONS

The mode shapes and pressure distributions at flutter for the horizontal-tail model as reported in NASA TN D-379 have been investigated analytically by the kernel-function method. The flutter mode shape was assumed to be a combination of the first three natural modes of the model. The results of this analysis indicate:

1. The contribution to the flutter mode of the third natural mode decreases as Mach number increases from 0.50 to 0.90.
2. The pressure distributions indicate that the size and location of the regions of the tail which contribute to the flutter instability by absorbing energy from the airstream are virtually unaffected by Mach number  $M$  in the range  $0.50 \leq M \leq 0.90$ .
3. The reduction in flutter frequency with increasing Mach number which had previously been observed in NASA TN D-379 for this tail results from a reduction in the aerodynamic stiffness forces.

Langley Research Center,  
National Aeronautics and Space Administration,  
Langley Air Force Base, Va., January 11, 1962.

L  
1  
2  
1  
8

## REFERENCES

1. Walberg, Gerald D.: Subsonic Kernel-Function Flutter Analysis of a Highly Tapered Tail Surface and Comparison With Experimental Results. NASA TN D-379, 1960.
2. Watkins, Charles E., Woolston, Donald S., and Cunningham, Herbert J.: A Systematic Kernel Function Procedure for Determining Aerodynamic Forces on Oscillating or Steady Finite Wings at Subsonic Speeds. NASA TR R-48, 1959.
3. Runyan, Harry L., and Woolston, Donald S.: Method for Calculating the Aerodynamic Loading on an Oscillating Finite Wing in Subsonic and Sonic Flow. NACA Rep. 1322, 1957. (Supersedes NACA TN 3694.)
4. Woolston, Donald S., and Sewall, John L.: Use of the Kernel Function in a Three-Dimensional Flutter Analysis With Application to a Flutter-Tested Delta-Wing Model. NACA TN 4395, 1958.

L  
1  
2  
1  
8

L  
1  
2  
1  
8

L  
1  
2  
1  
8

TABLE I.- PROPERTIES OF MODEL

Thickness ratio . . . . .	0.035
Leading-edge sweep angle, $\Lambda_{le}$ , deg . . . . .	30
Streamwise airfoil section . . . . .	Biconvex
Streamwise semichord at center line, $b_0$ , ft . . . . .	0.625
Semispan, $l$ , ft . . . . .	1.220
Panel mass, lb-sec <sup>2</sup> /ft . . . . .	0.05579
Panel aspect ratio, $A_p$ . . . . .	1.66
Taper ratio, $\lambda$ . . . . .	0.176
Natural frequencies, cps:	
First mode . . . . .	40
Second mode . . . . .	108
Third mode . . . . .	117

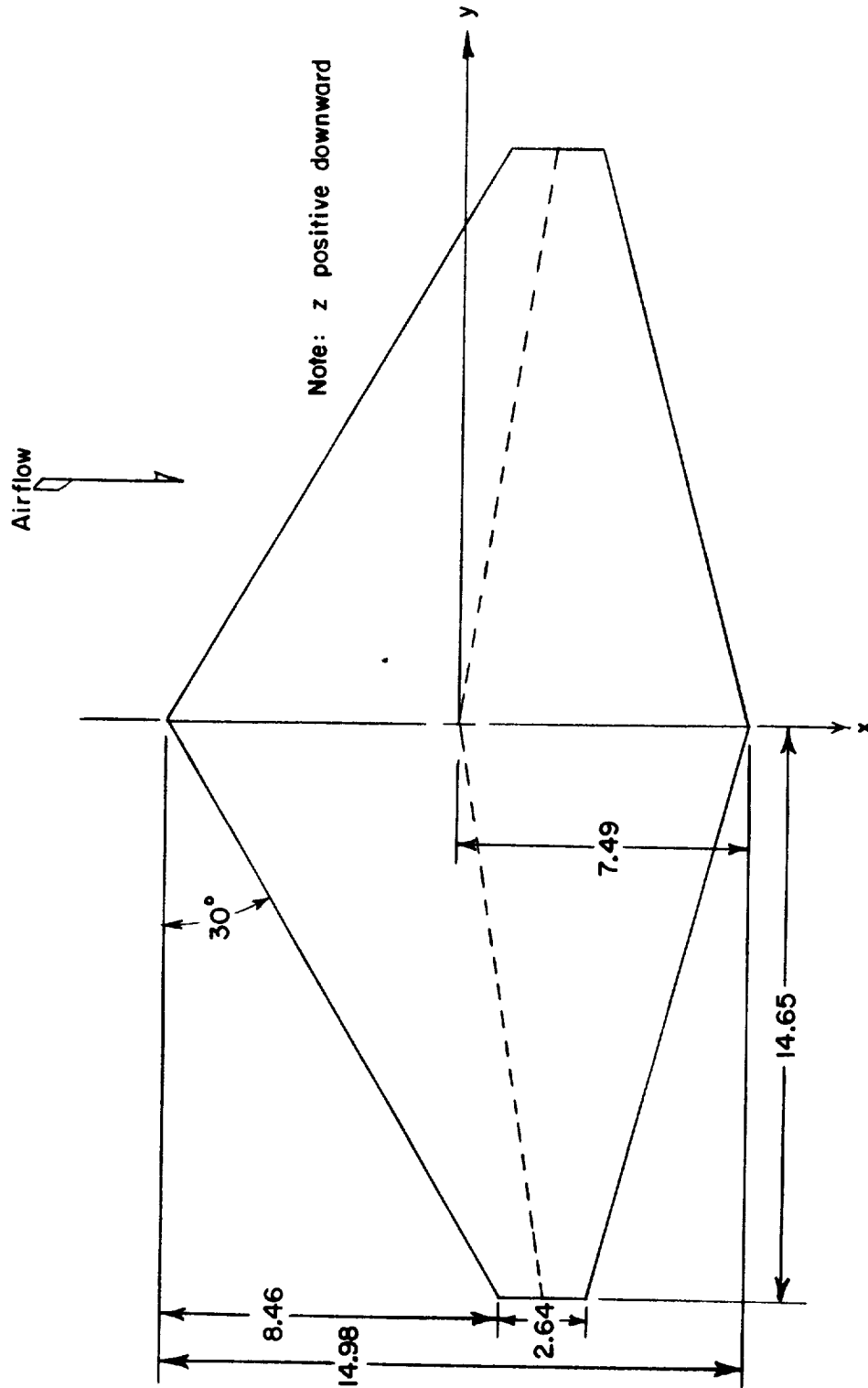
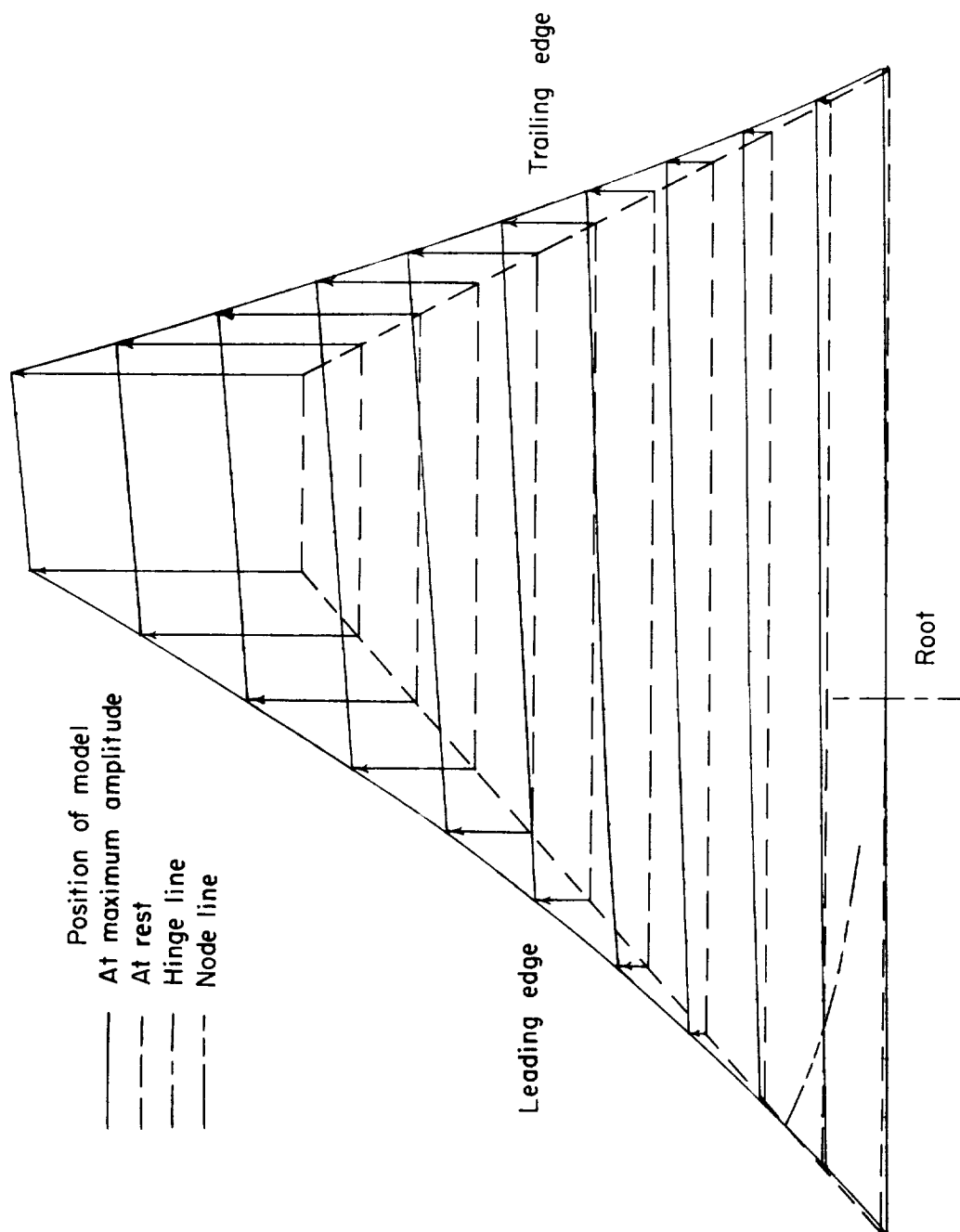
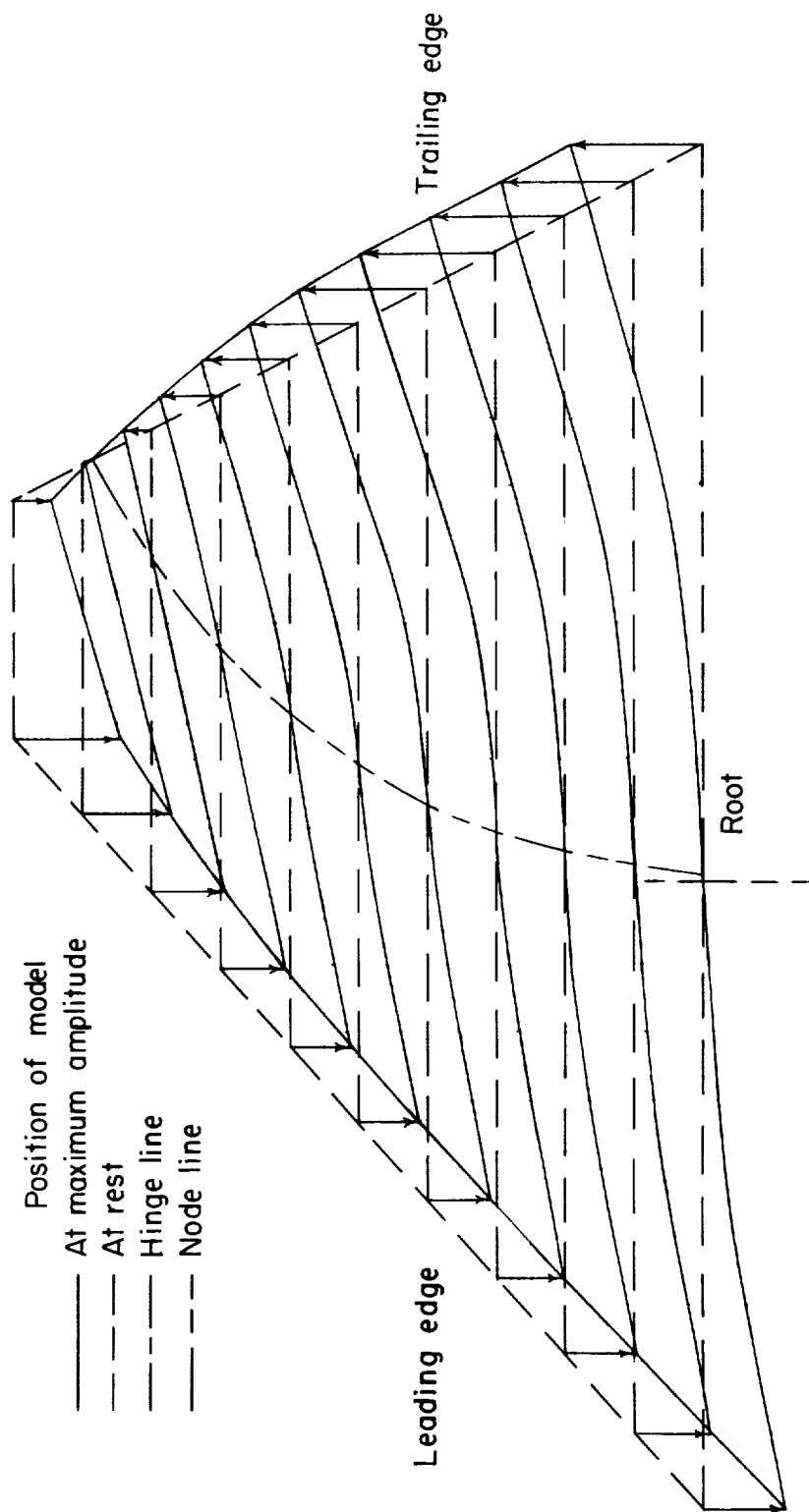


Figure 1.- Planform and coordinate system. All dimensions are in inches except as otherwise indicated.



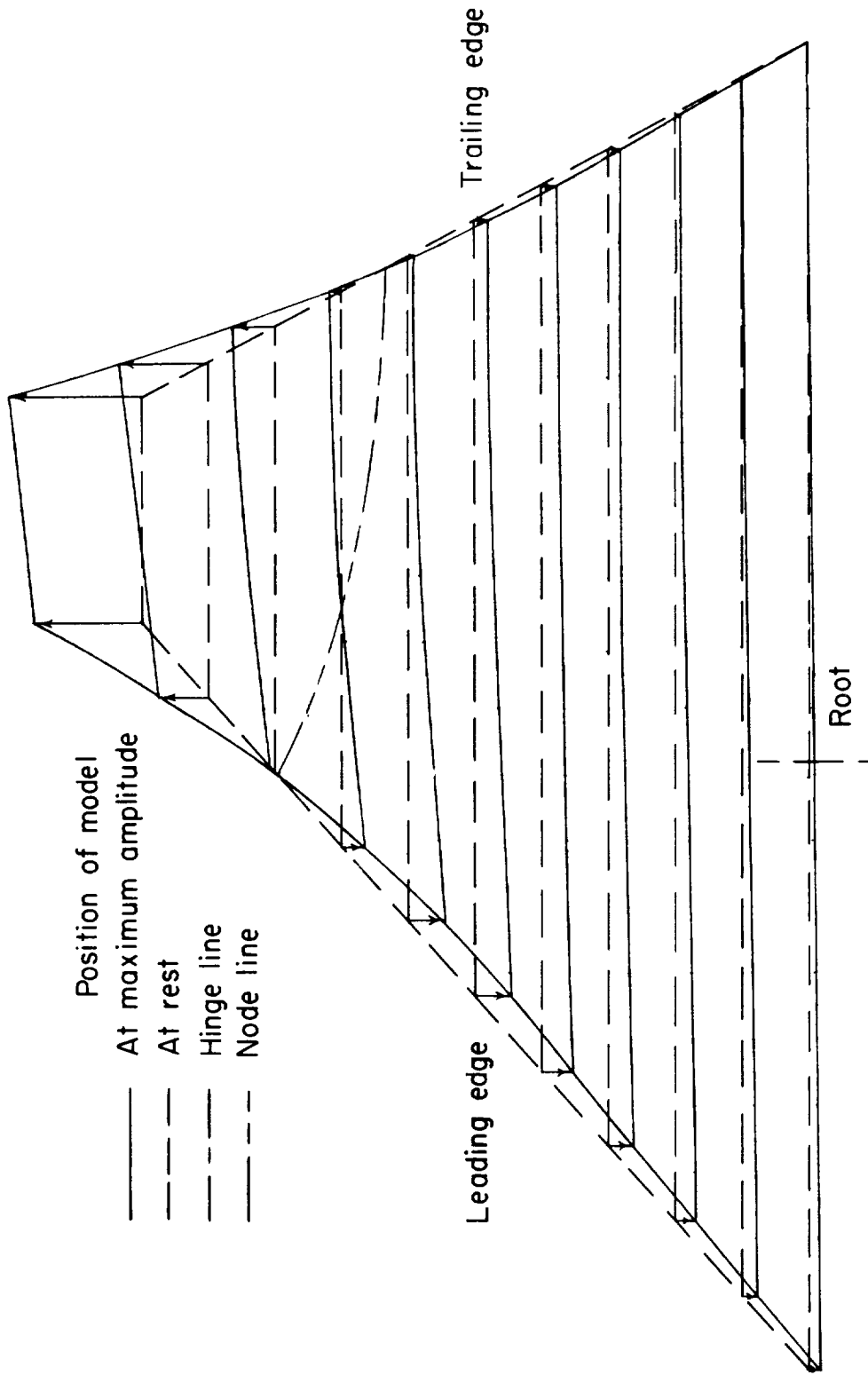
(a) First mode  $h_1$ .  $f_1 = 40$  cps.

Figure 2.- Measured natural mode shapes for model.



(b) Second mode  $h_2$ .  $f_2 = 108$  cps.

Figure 2.- Continued.



(c) Third mode  $h_3$ .  $f_3 = 117$  cps.

Figure 2.- Concluded.

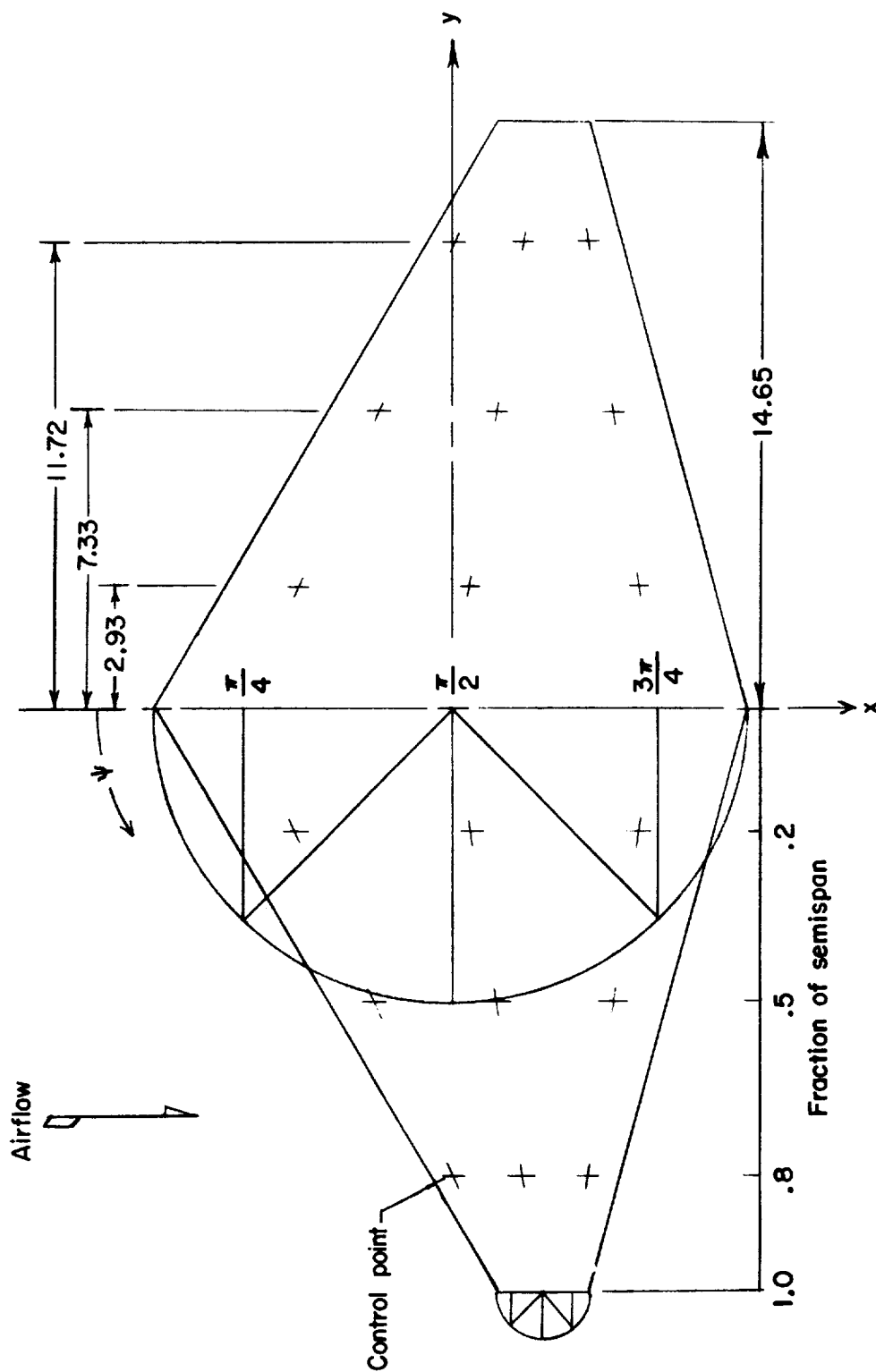


Figure 3.- Location of control points for kernel-function program. All dimensions are in inches except as otherwise indicated.

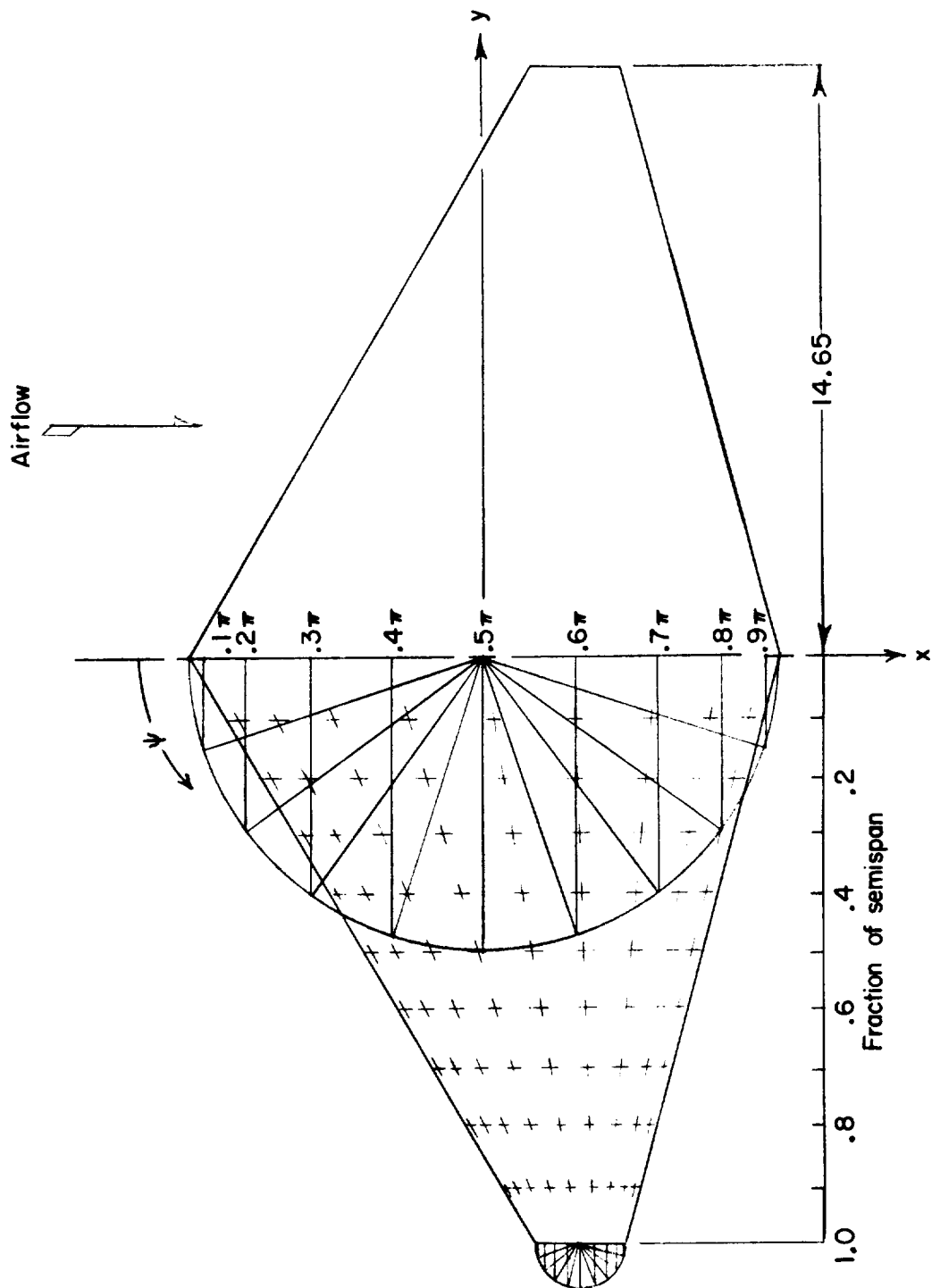


Figure 4.- Location of points for pressure distribution. All dimensions are in inches except as otherwise indicated.

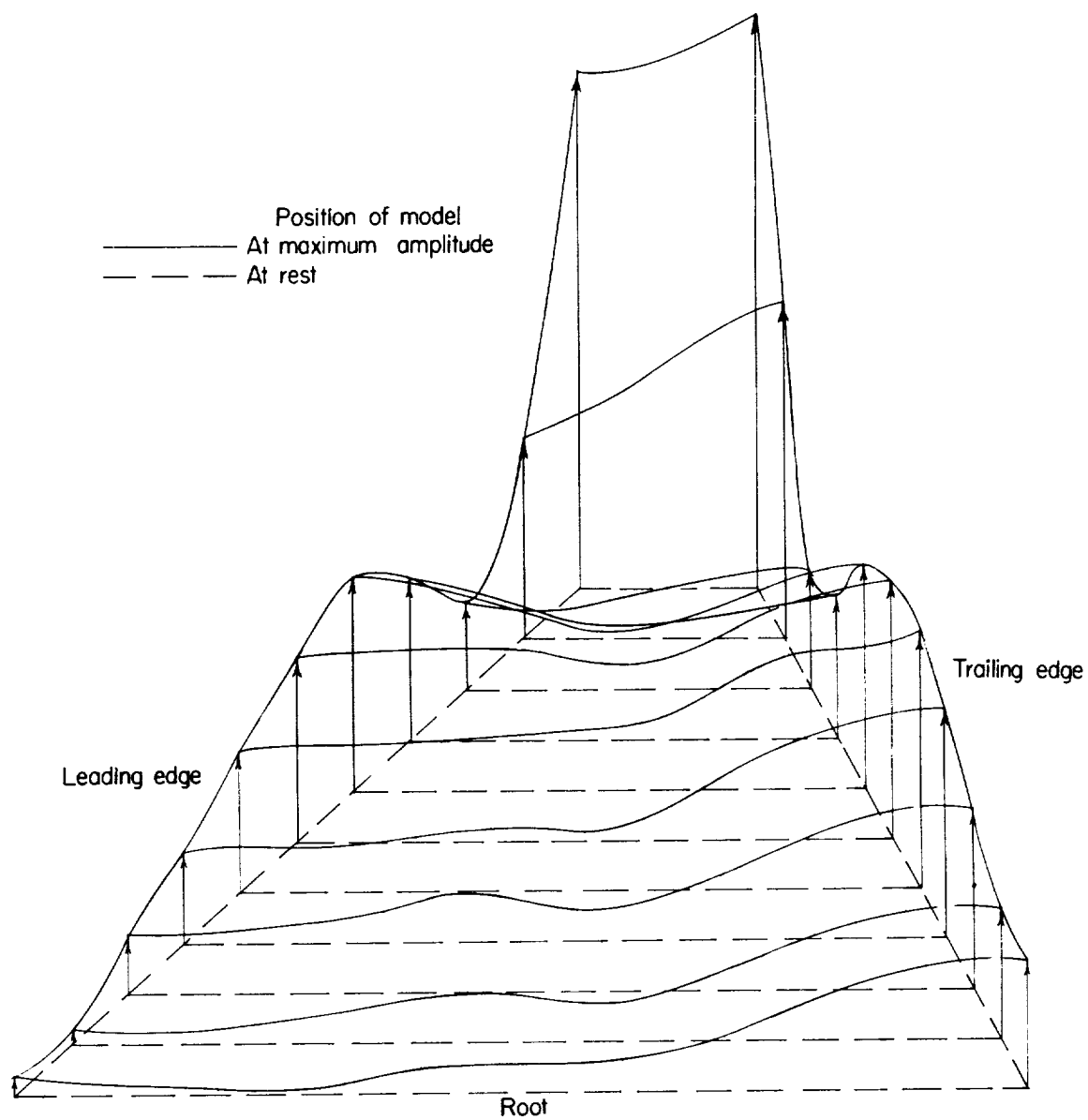
(a)  $M = 0.50$ .

Figure 5.- Maximum amplitude  $h_0(x,y)$  for flutter-mode shapes as defined in equation (10).

I-1218

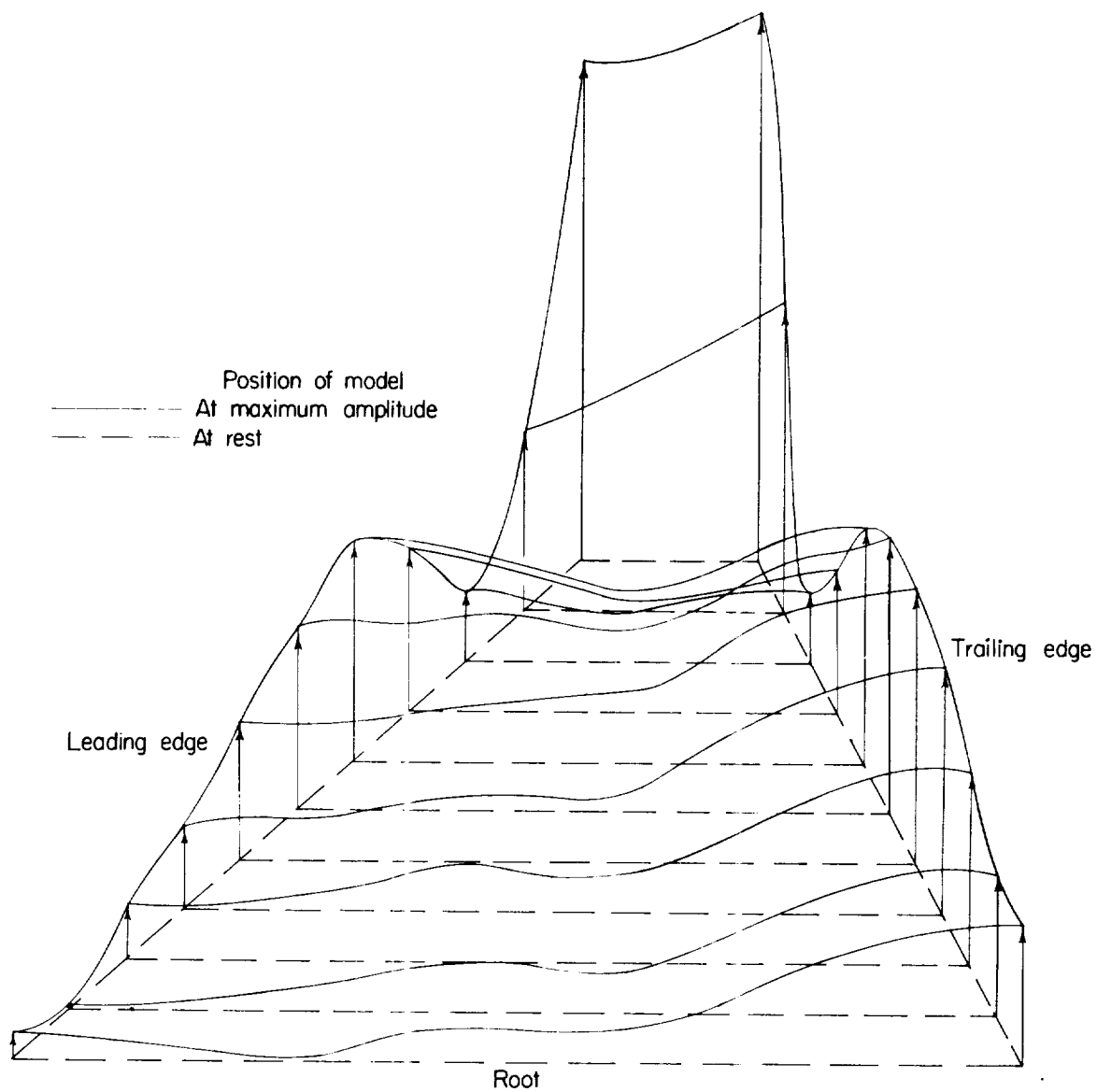
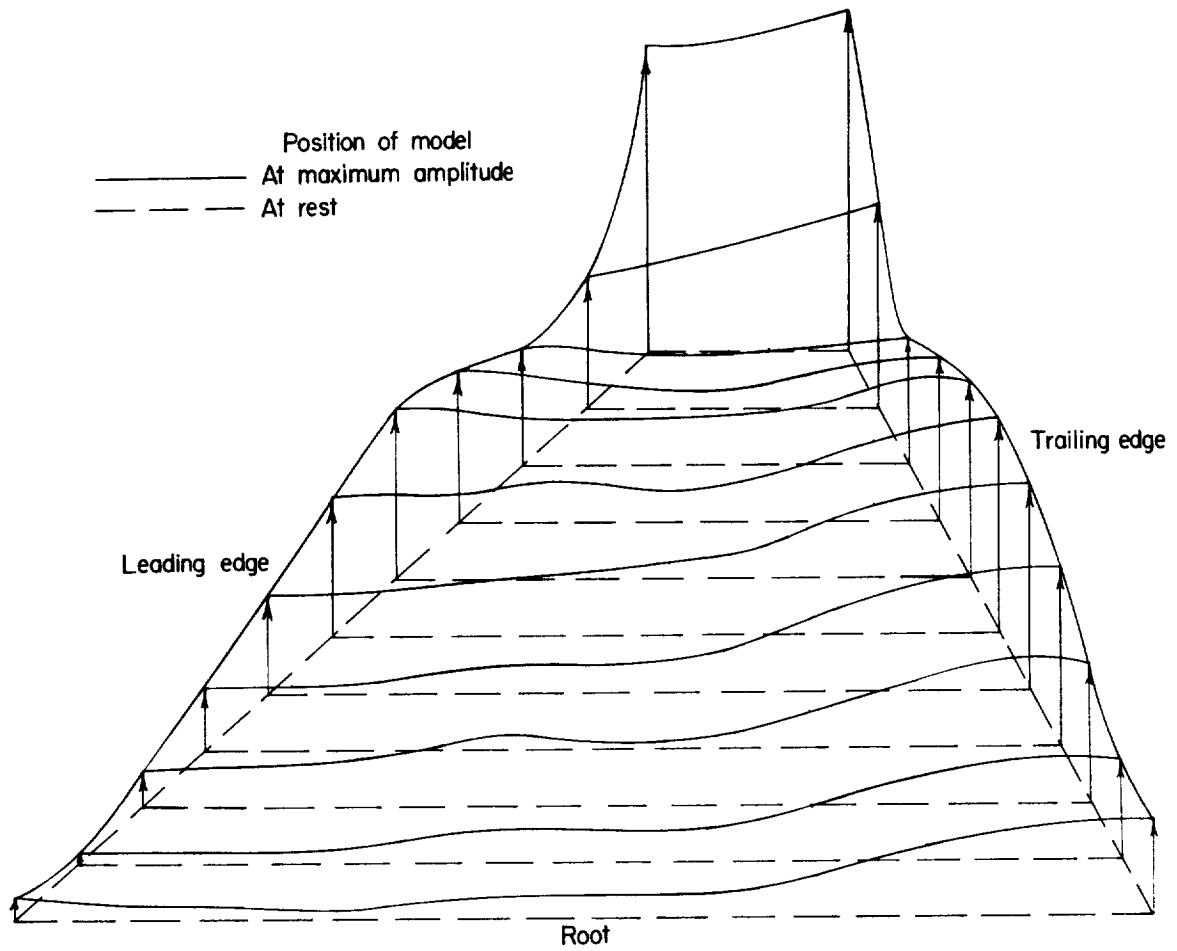
(b)  $M = 0.75$ .

Figure 5.- Continued.



(c)  $M = 0.80$ .

Figure 5.- Continued.

I-1218

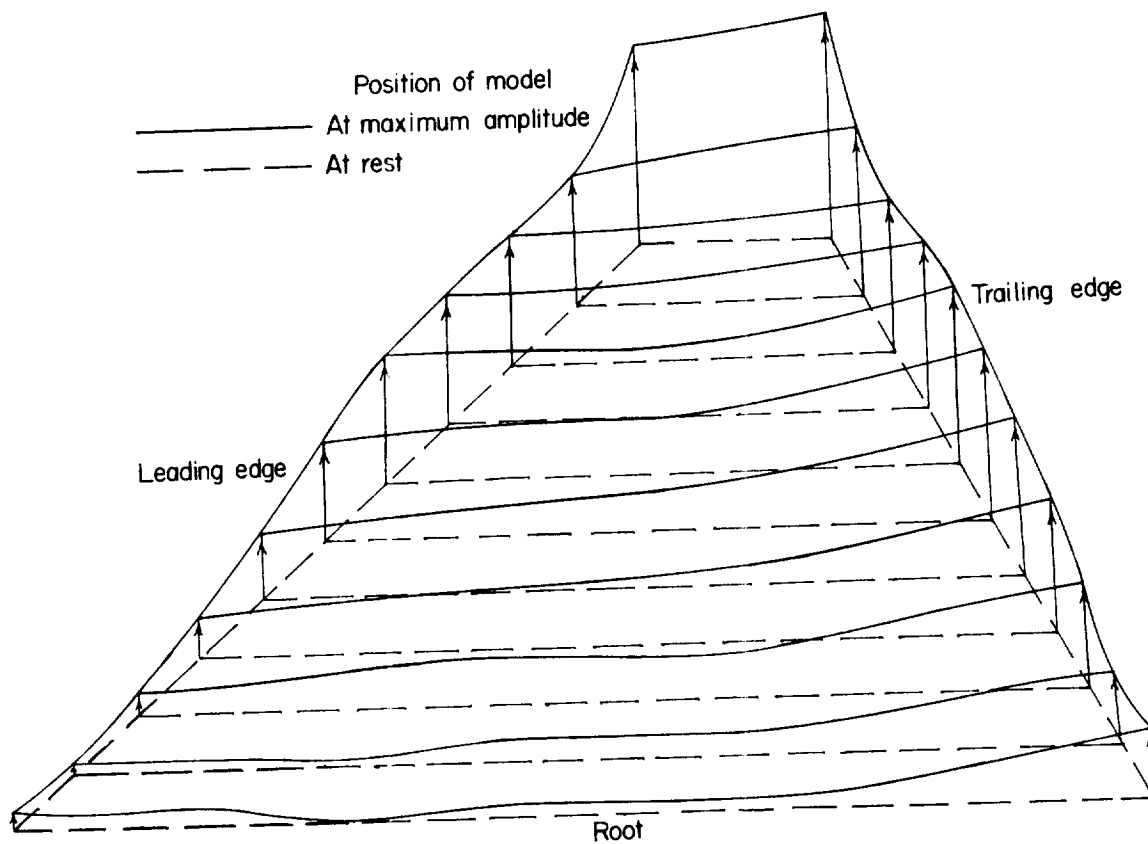
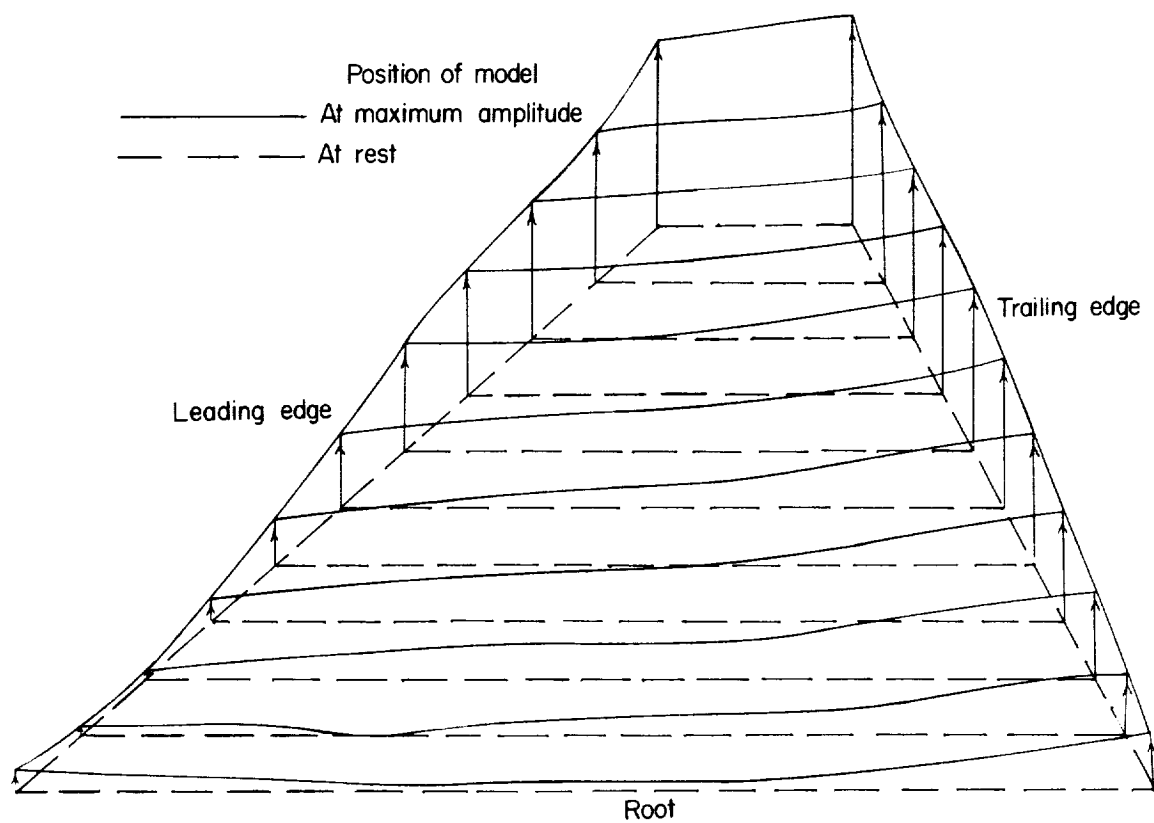
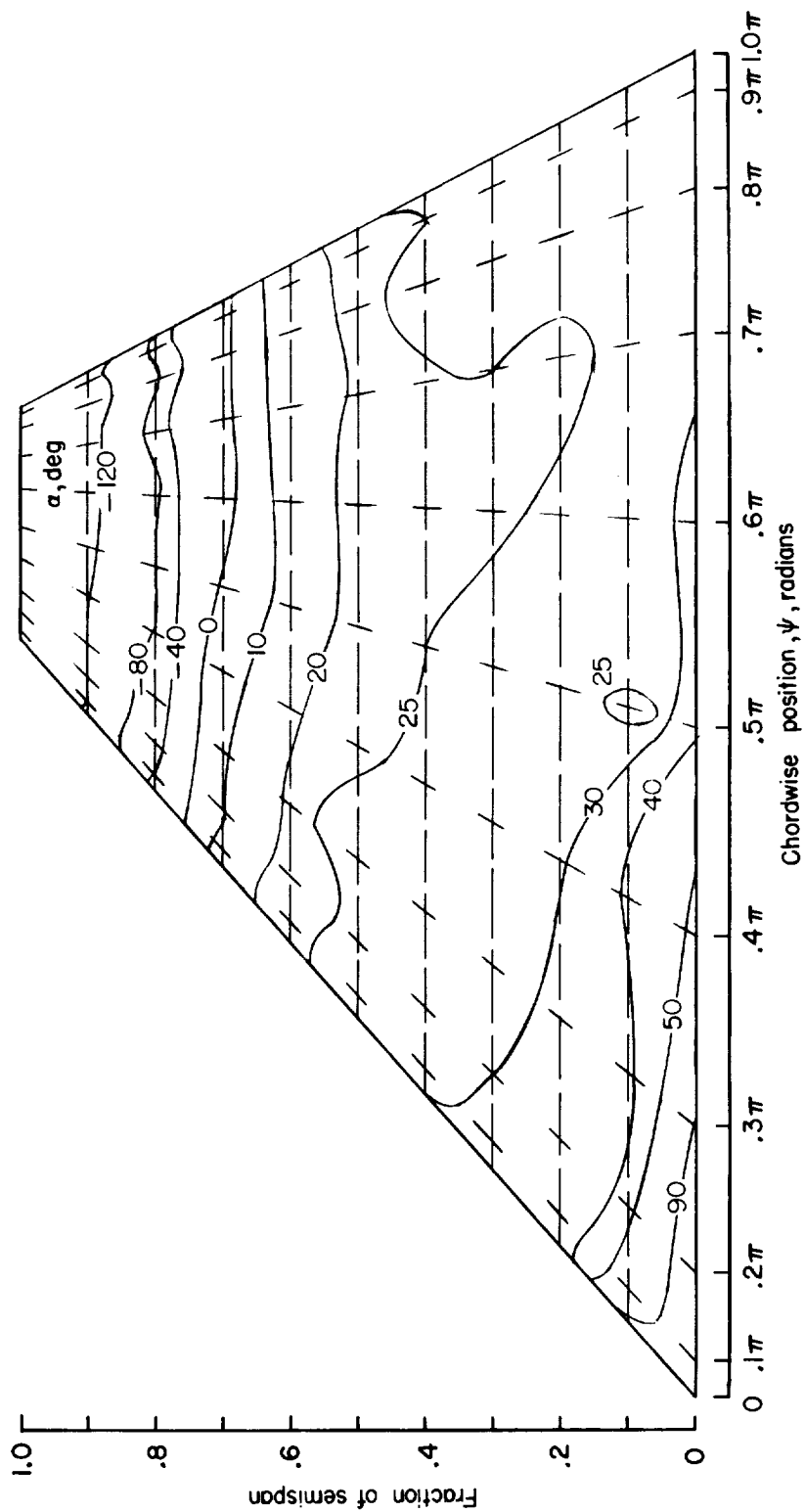
(d)  $M = 0.85$ .

Figure 5.- Continued.



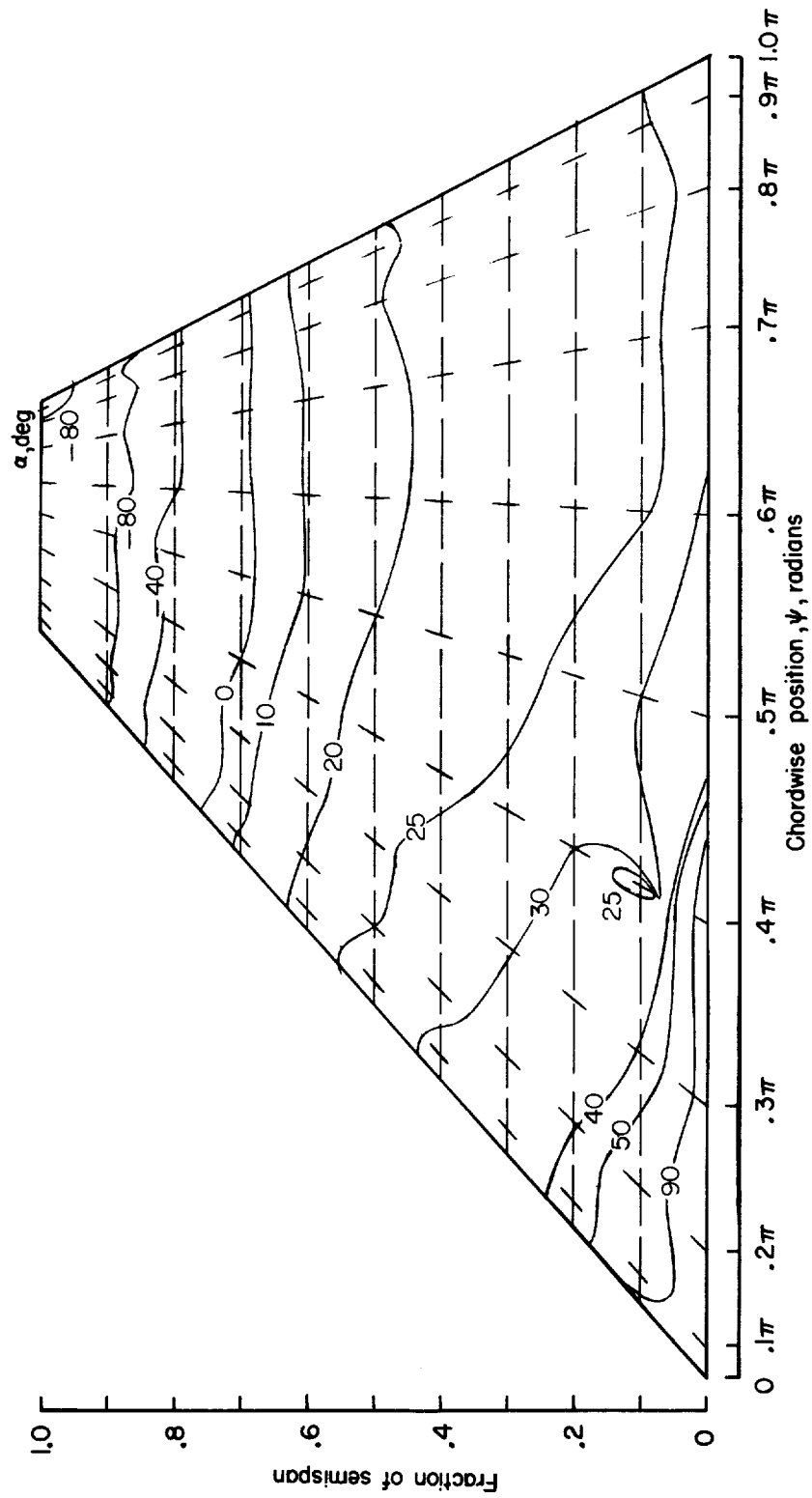
(e)  $M = 0.90$ .

Figure 5.- Concluded.



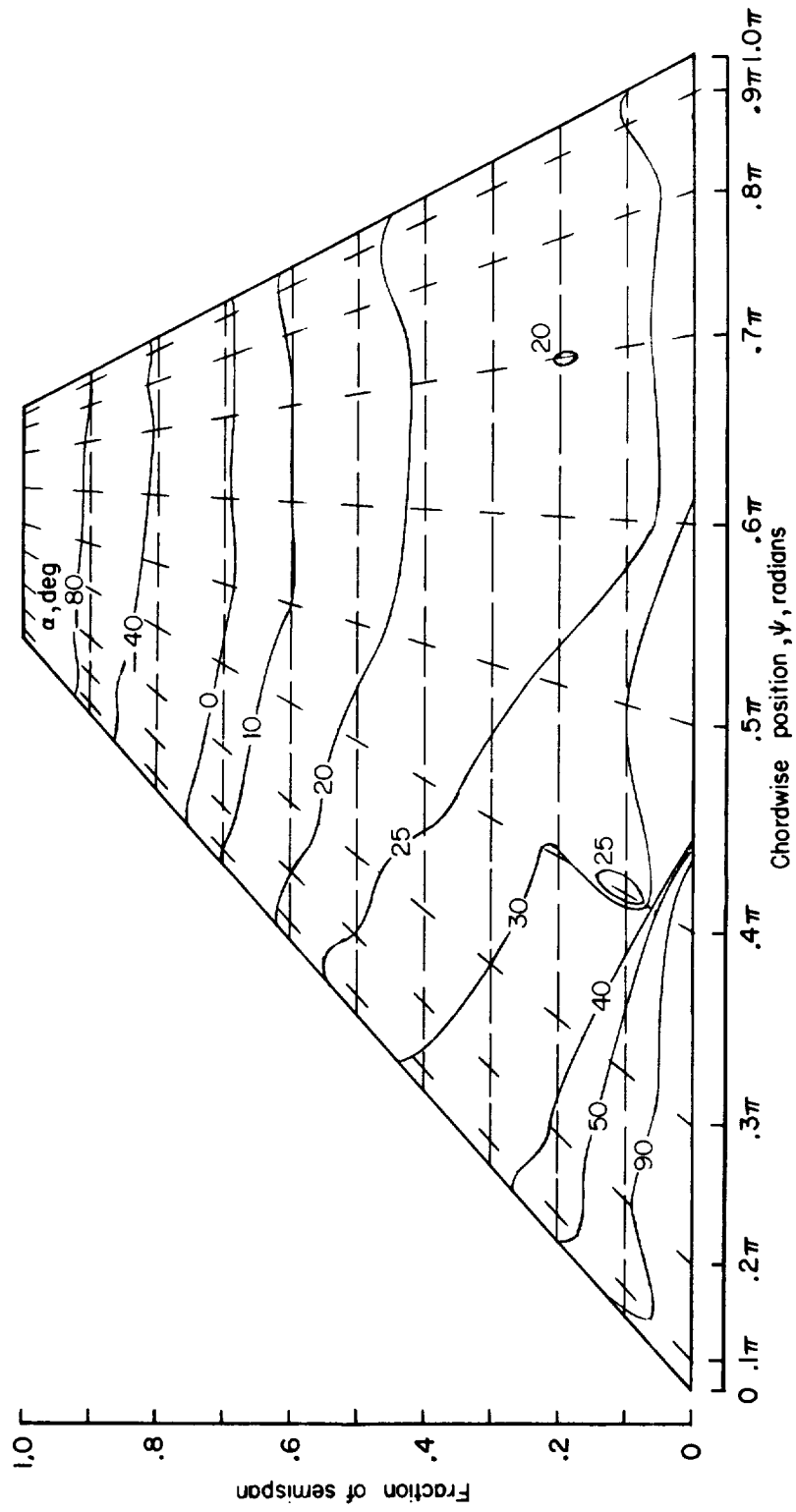
(a)  $M = 0.50$ ;  $k_0 = 0.254$ .

Figure 6.- Phase angle  $\alpha(x, y)$  between the displacement at flutter and its first natural-mode component.



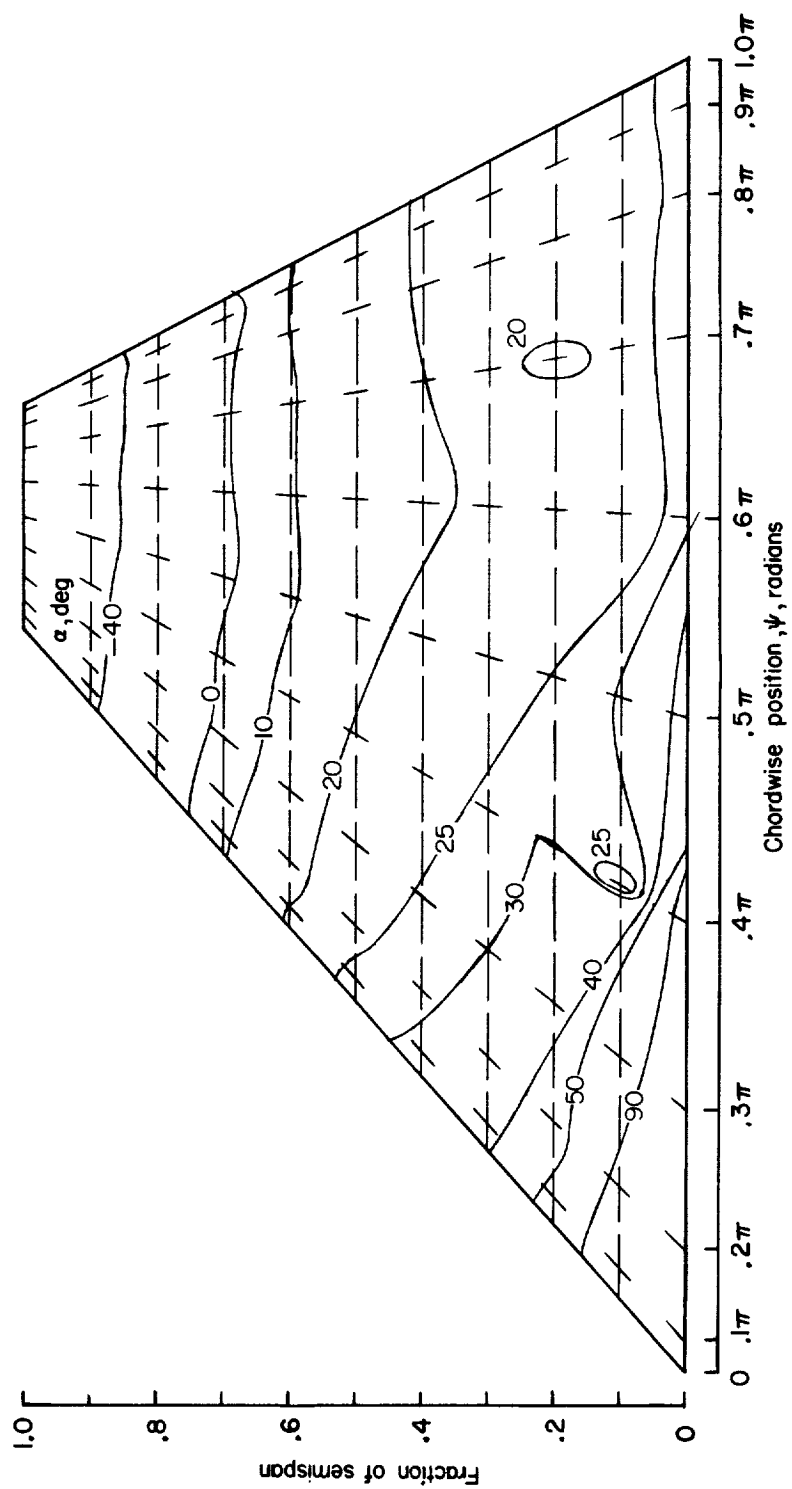
(b)  $M = 0.75$ ;  $k_0 = 0.254$ .

Figure 6.- Continued.



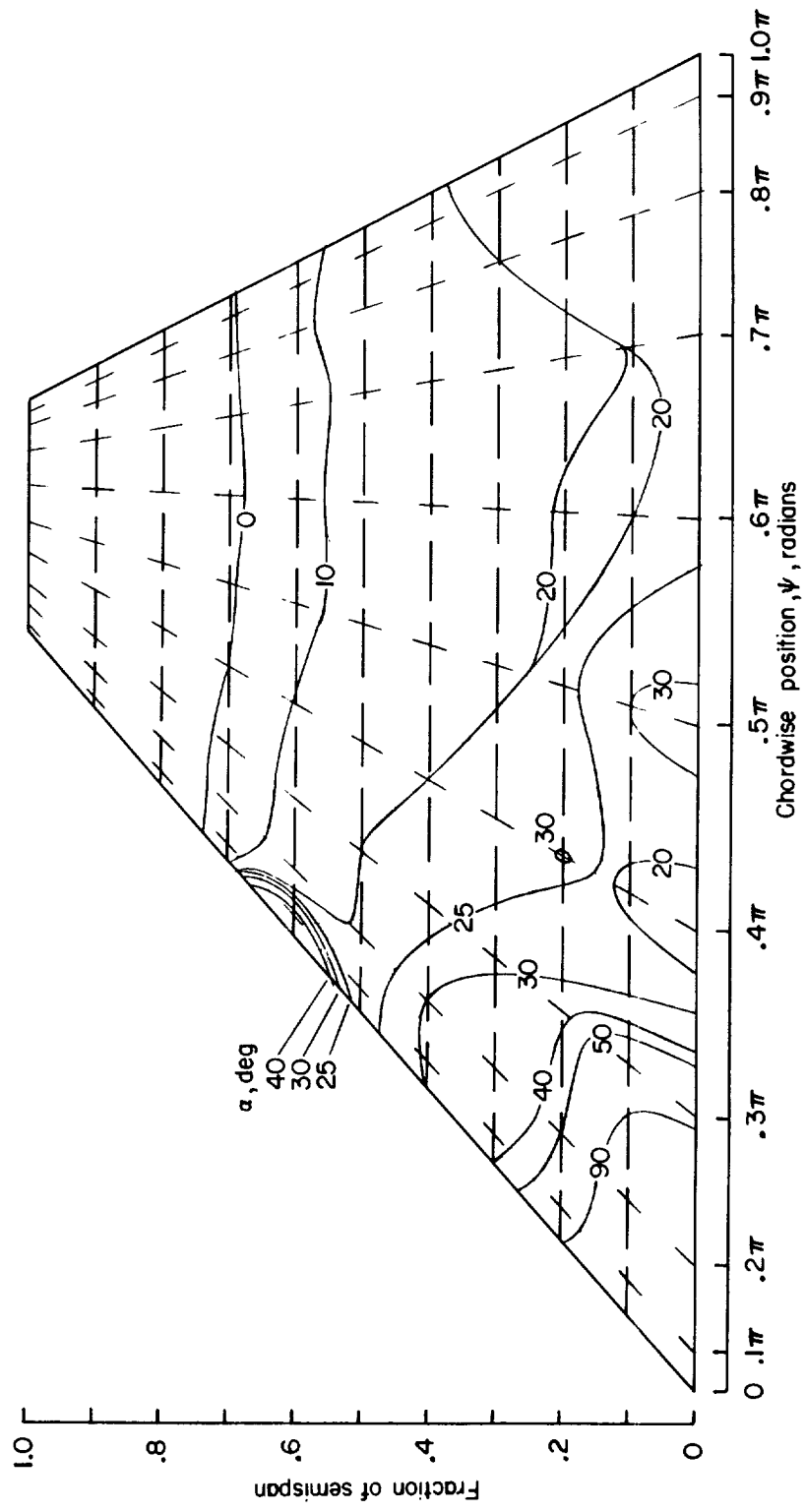
(c)  $M = 0.80$ ;  $k_0 = 0.2525$ .

Figure 6.- Continued.



(d)  $M = 0.85$ ;  $k_0 = 0.248$ .

Figure 6.- Continued.



(e)  $M = 0.90$ ;  $k_0 = 0.245$ .

Figure 6.- Concluded.

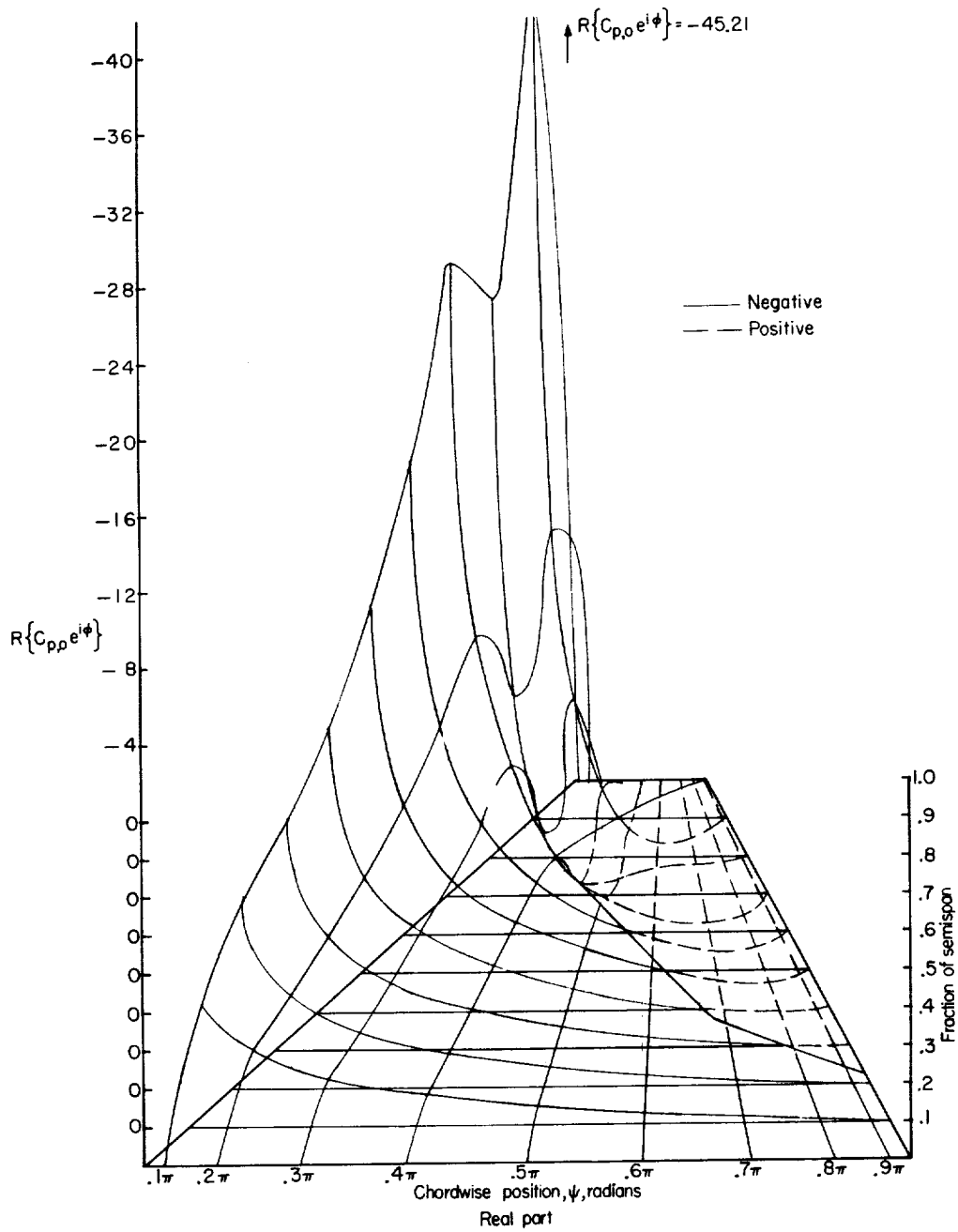
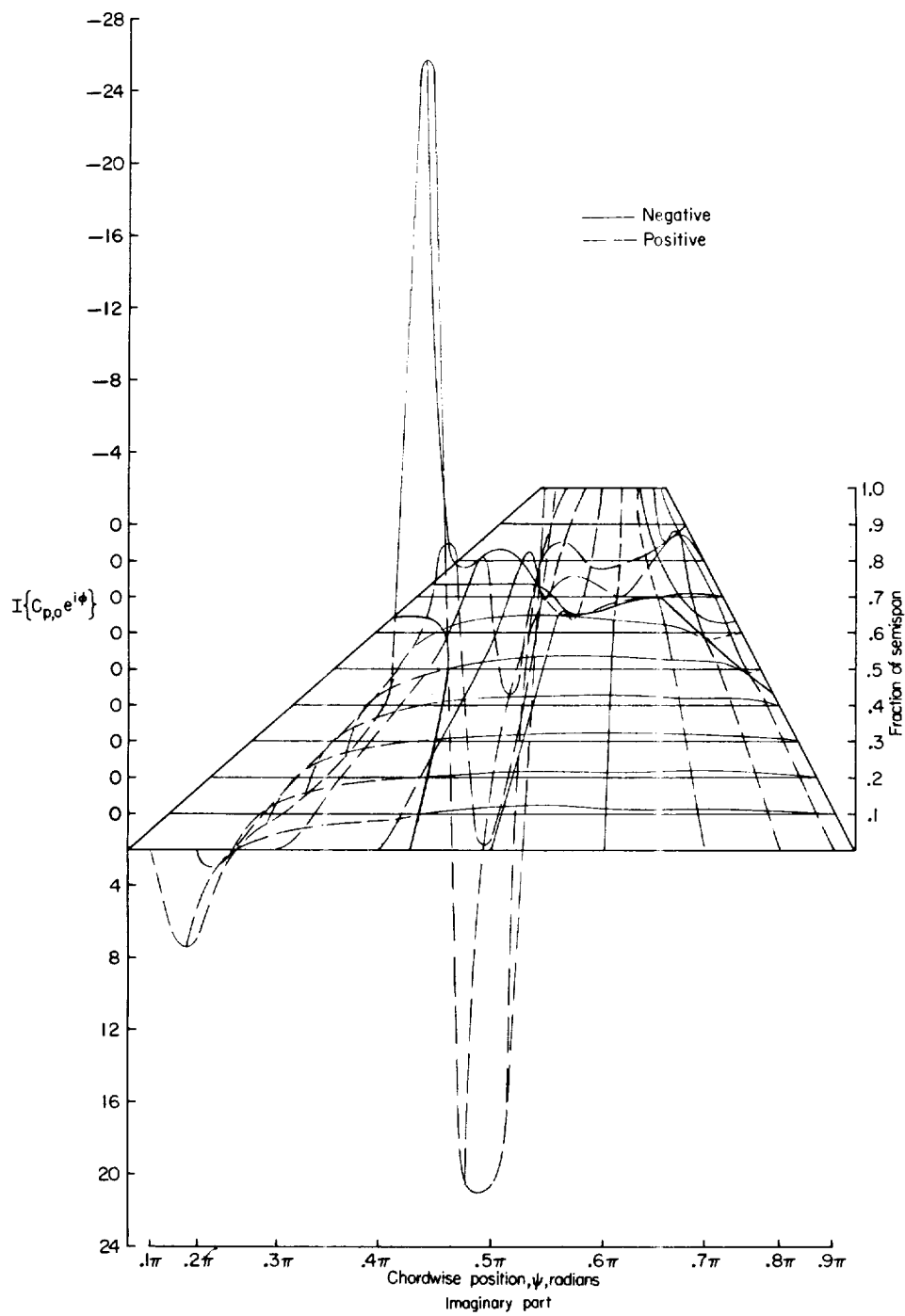
(a)  $M = 0.50$ ;  $k_0 = 0.245$ .

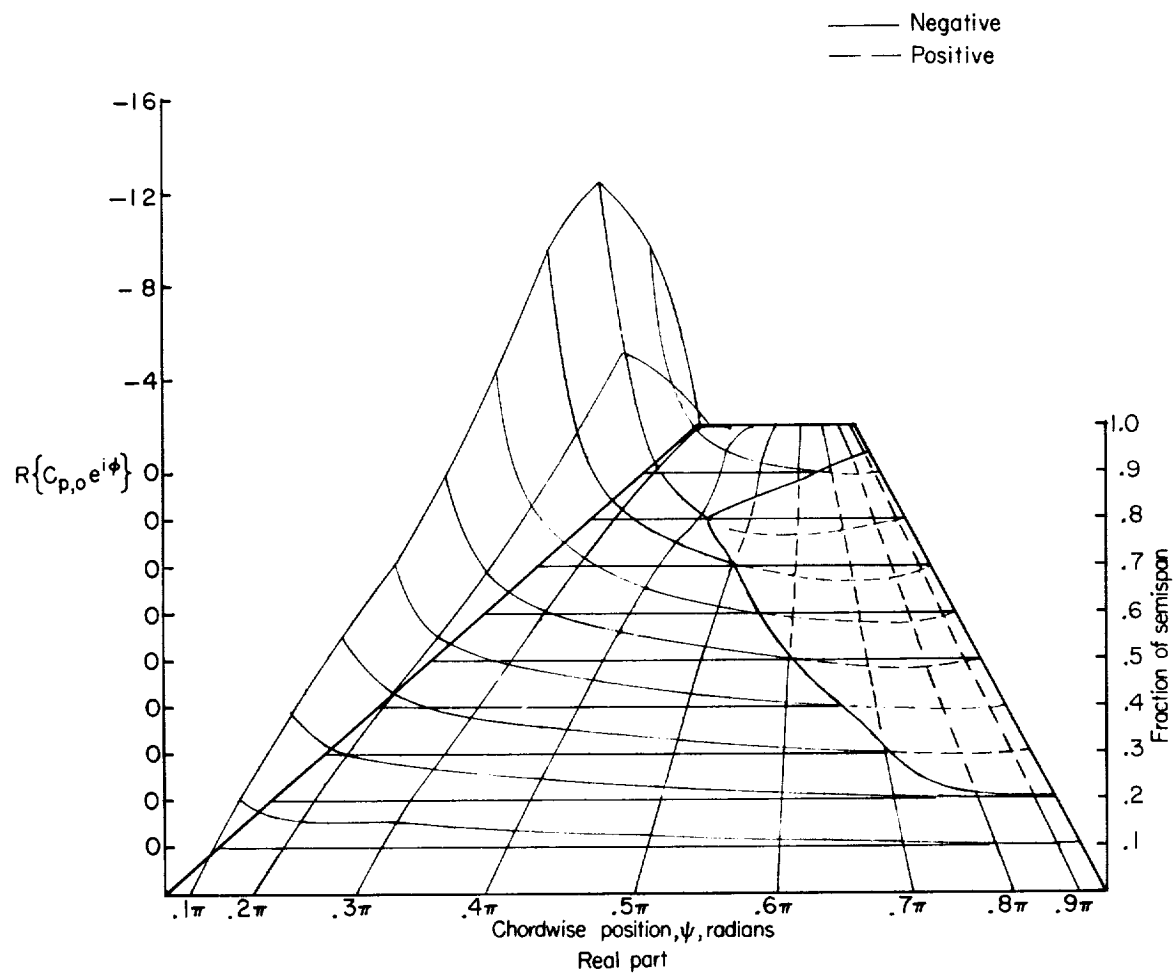
Figure 7.- Complex amplitude  $C_{p,0}e^{i\phi}$  of the lifting-pressure coefficient referred to the flutter displacement. (See eq. (14).)

L-1218



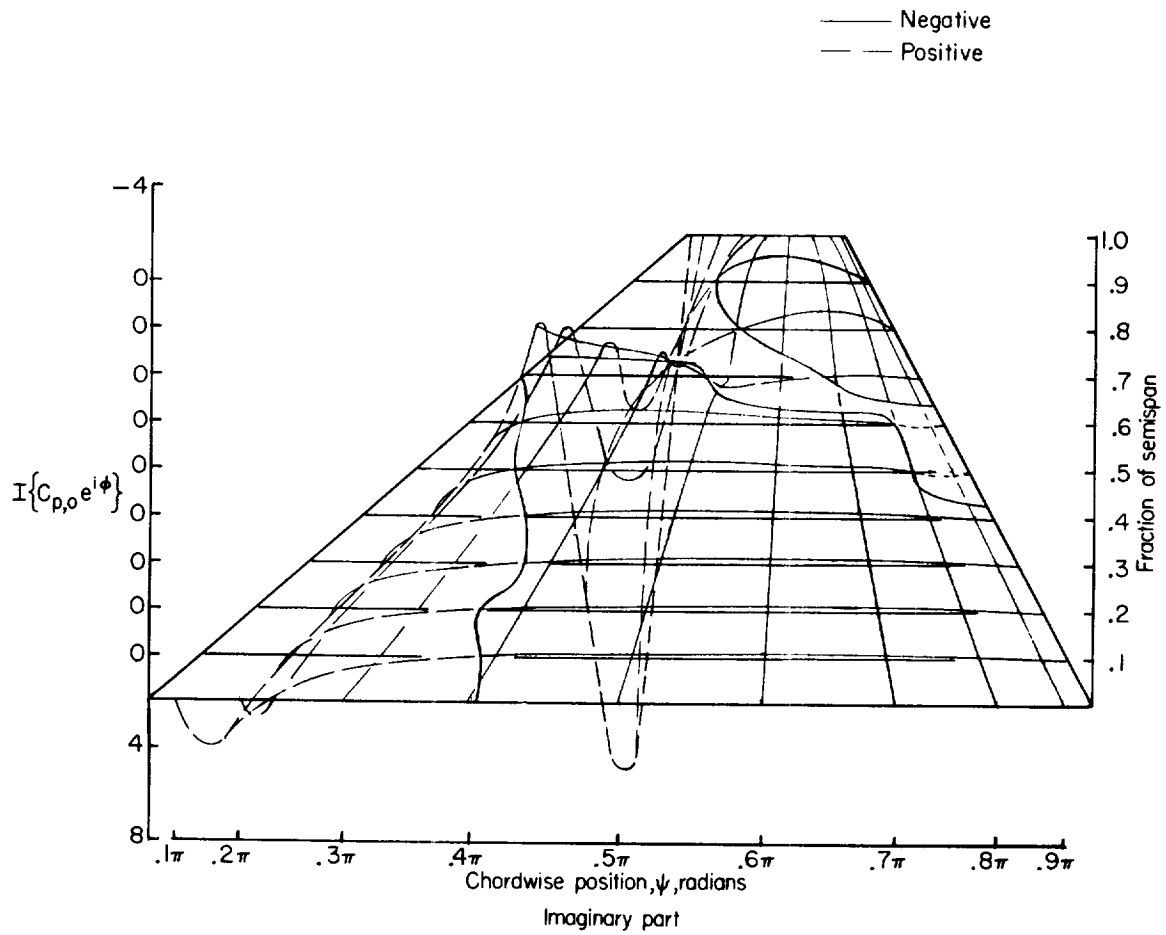
(a) Concluded.

Figure 7.- Continued.



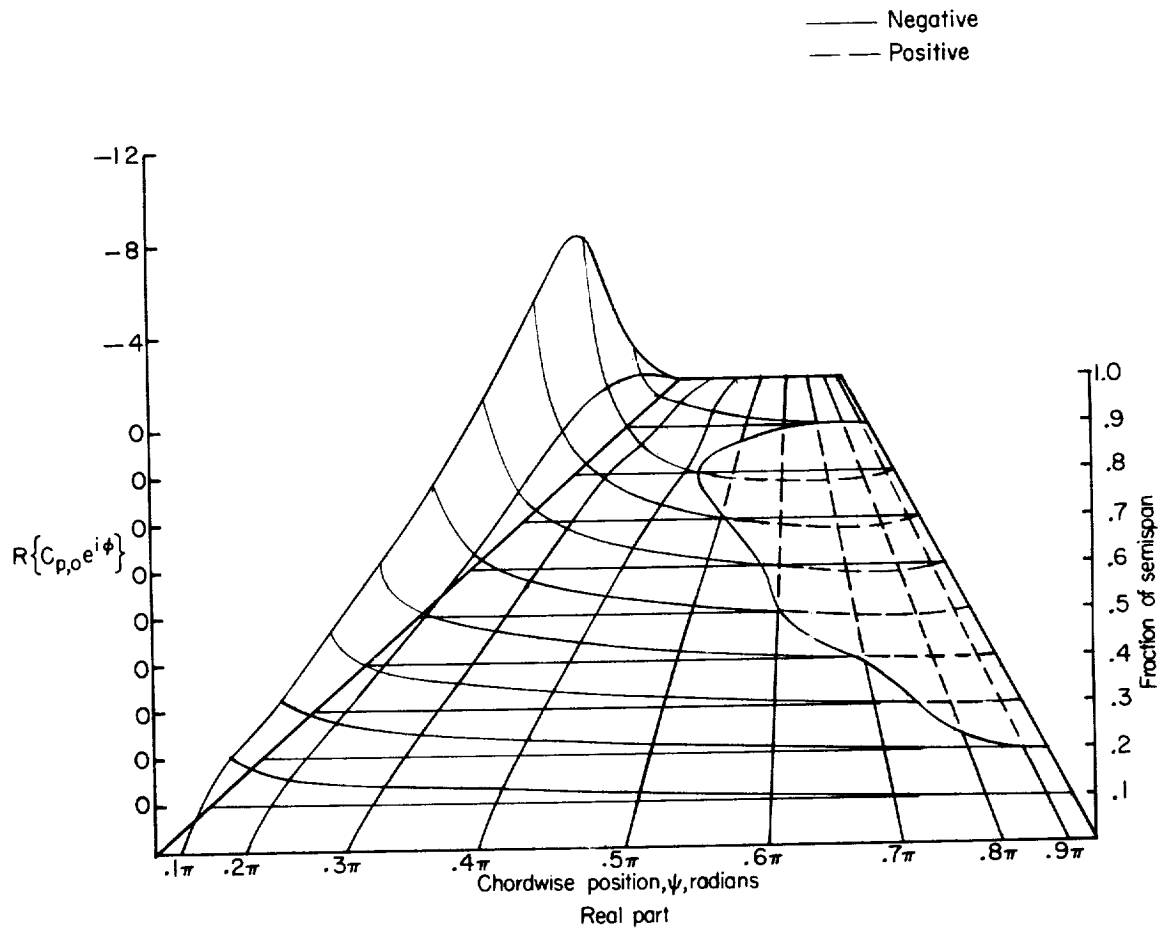
(b)  $M = 0.75$ ;  $k_0 = 0.254$ .

Figure 7.- Continued.



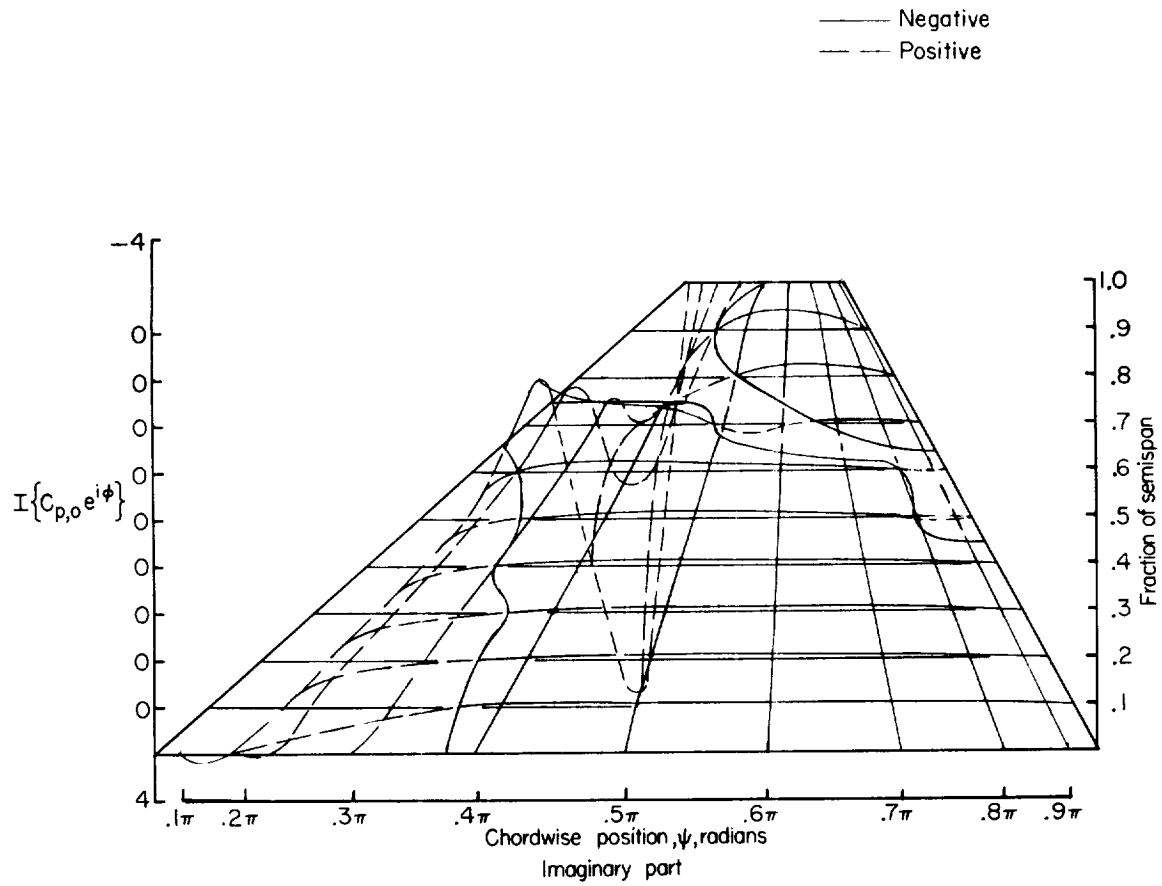
(b) Concluded.

Figure 7.- Continued.



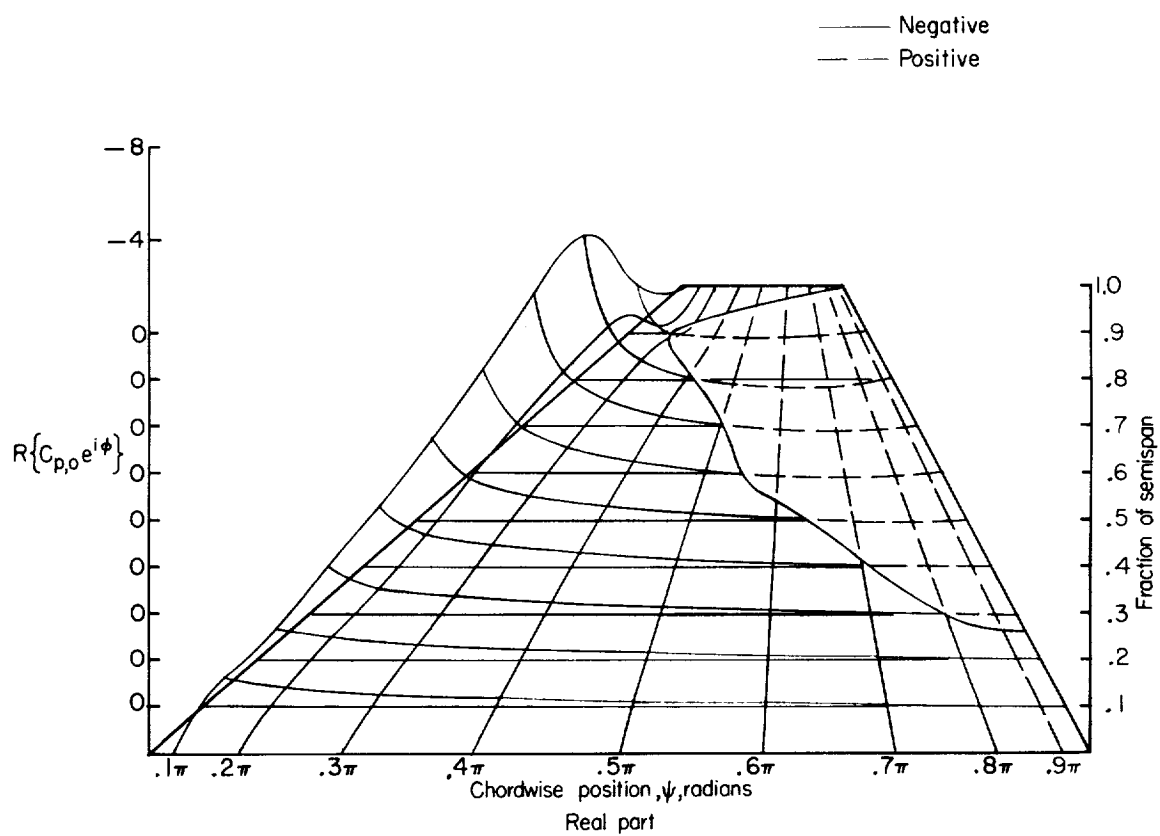
(c)  $M = 0.80$ ;  $k_0 = 0.2525$ .

Figure 7.- Continued.



(c) Concluded.

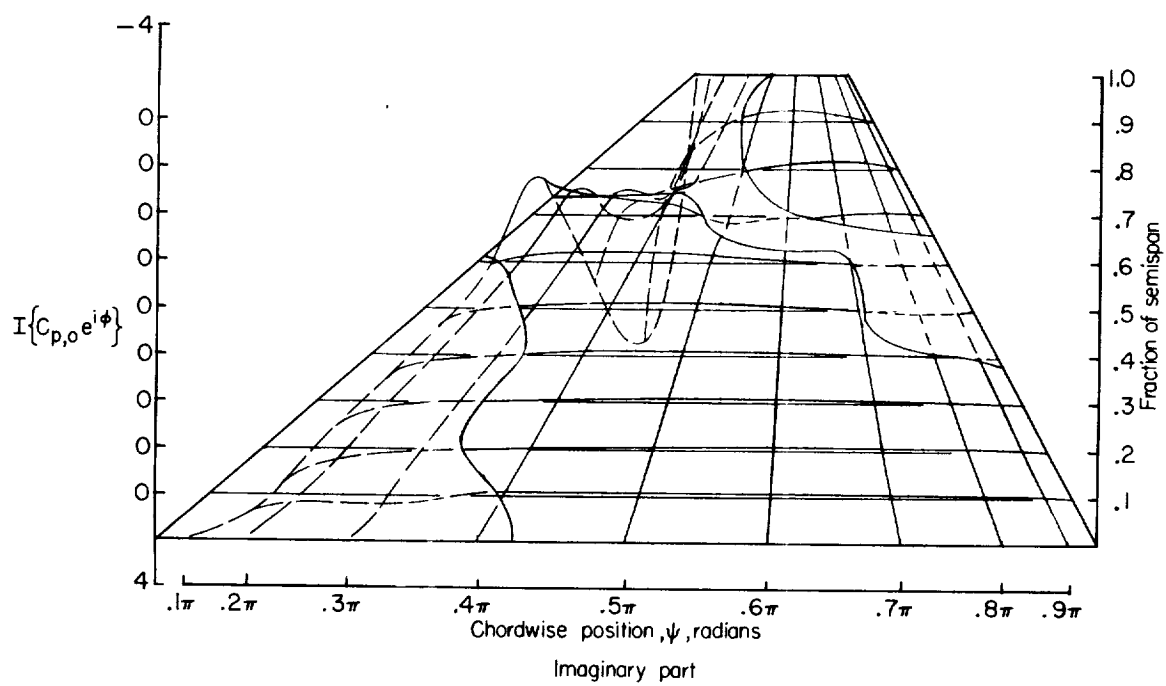
Figure 7.- Continued.



(d)  $M = 0.85$ ;  $k_0 = 0.248$ .

Figure 7.- Continued.

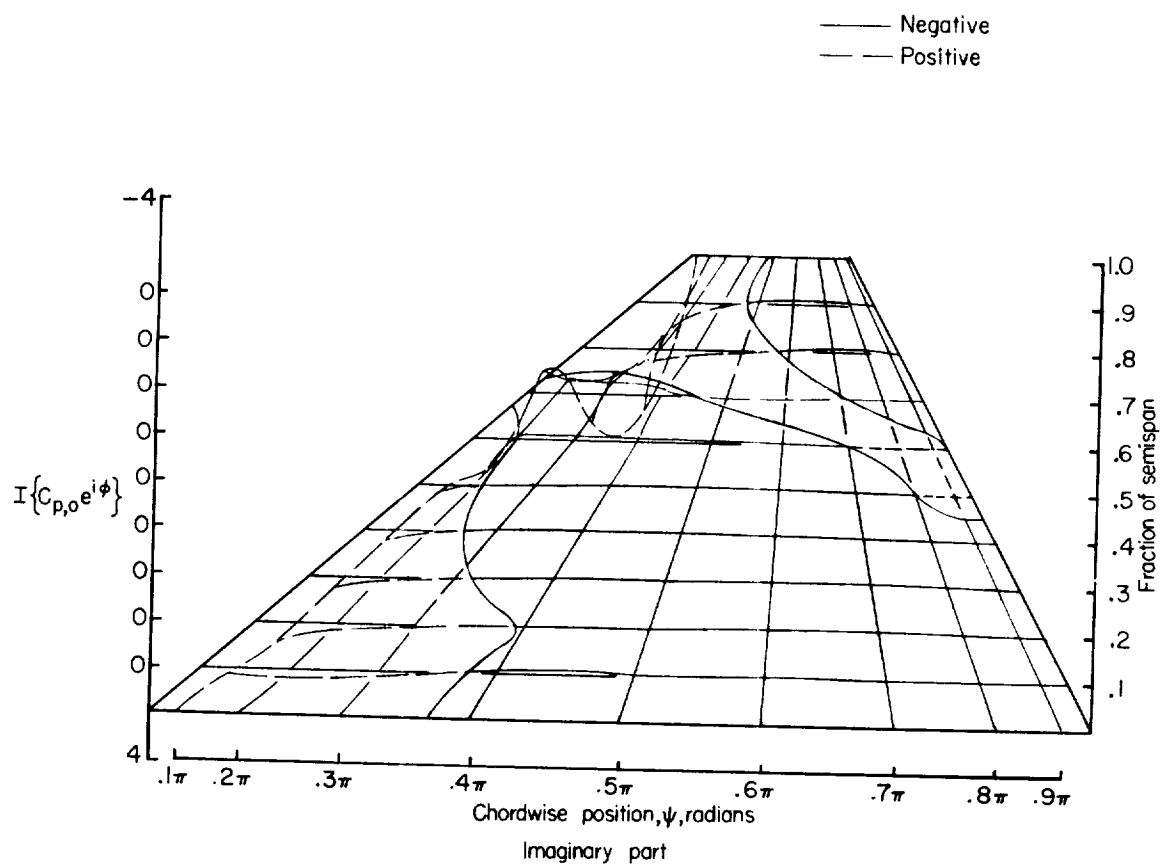
— Negative  
 - - - Positive



(d) Concluded.

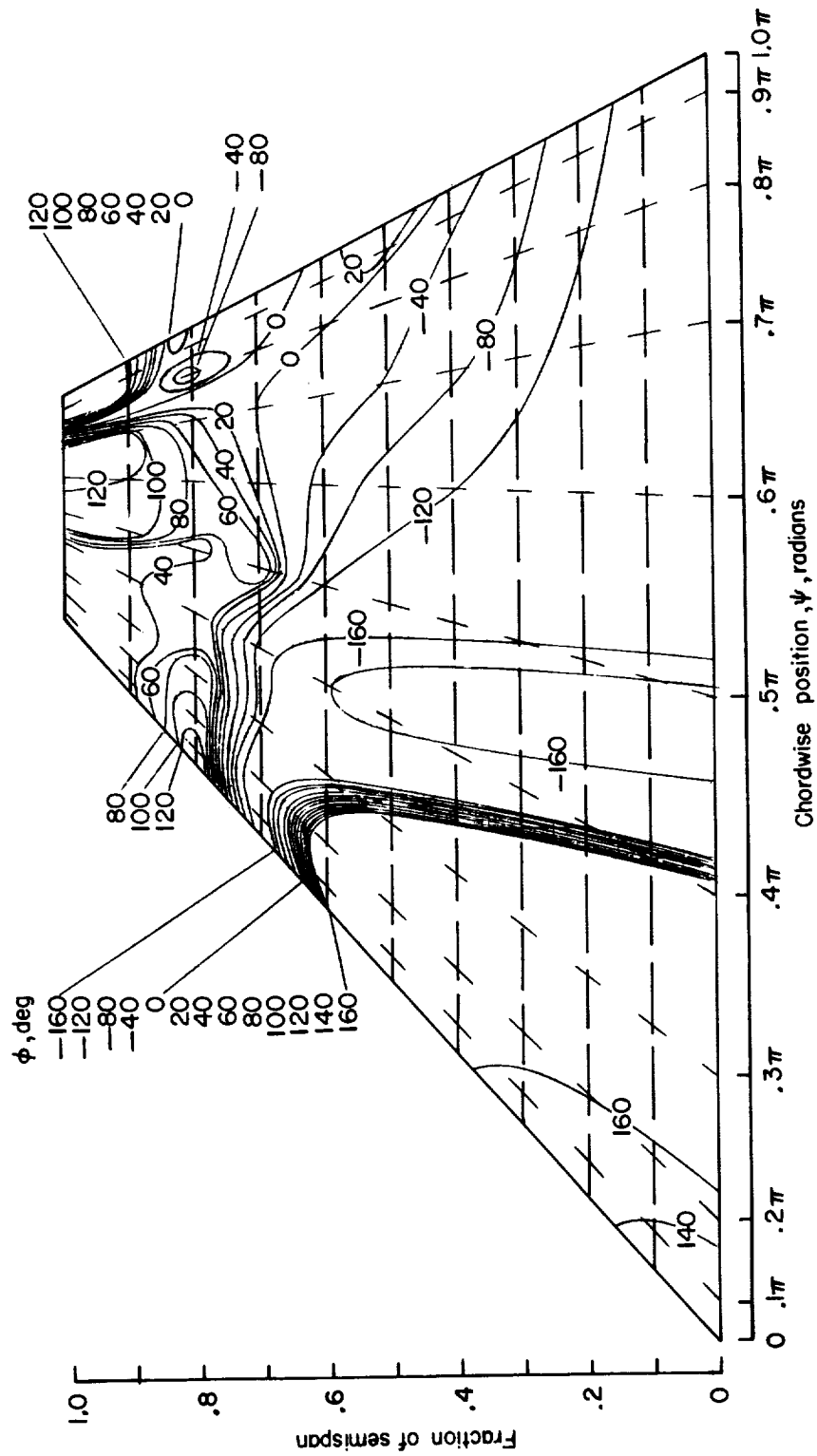
Figure 7.- Continued.





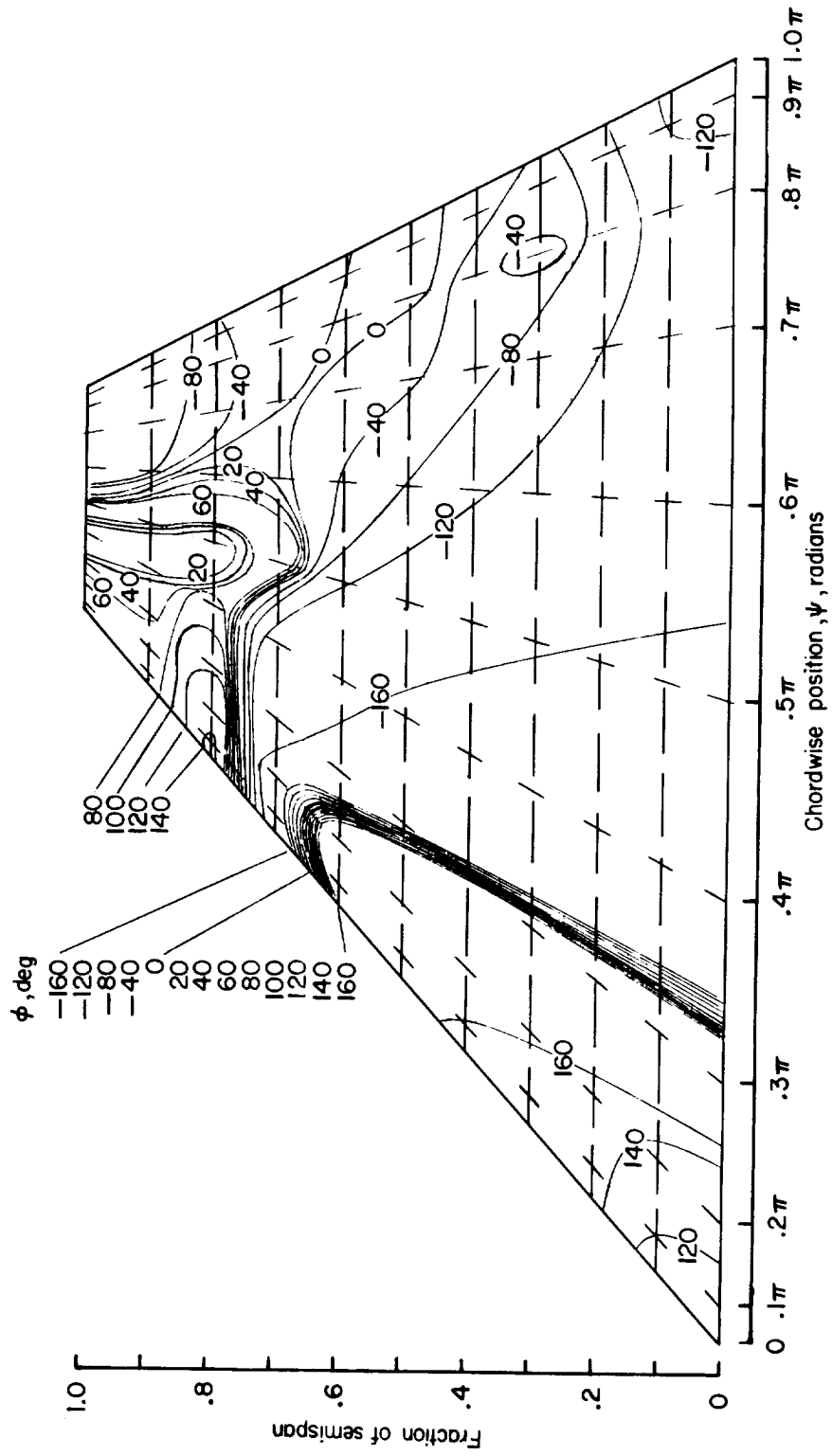
(e) Concluded.

Figure 7.- Concluded.



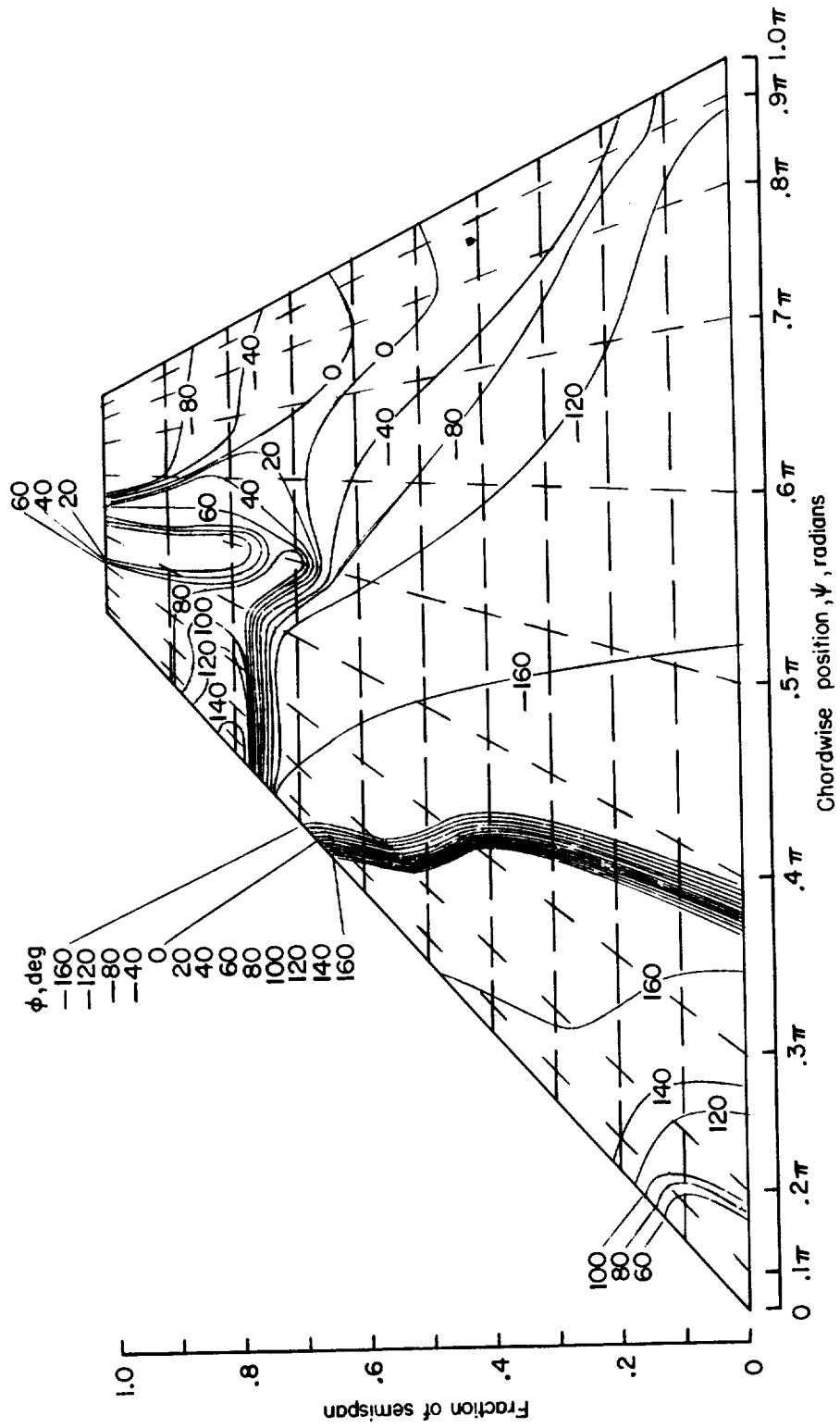
(a)  $M = 0.50$ ;  $k_0 = 0.254$ .

Figure 8.- Phase angle  $\phi(x, y)$  between lifting-pressure coefficient and displacement at flutter.



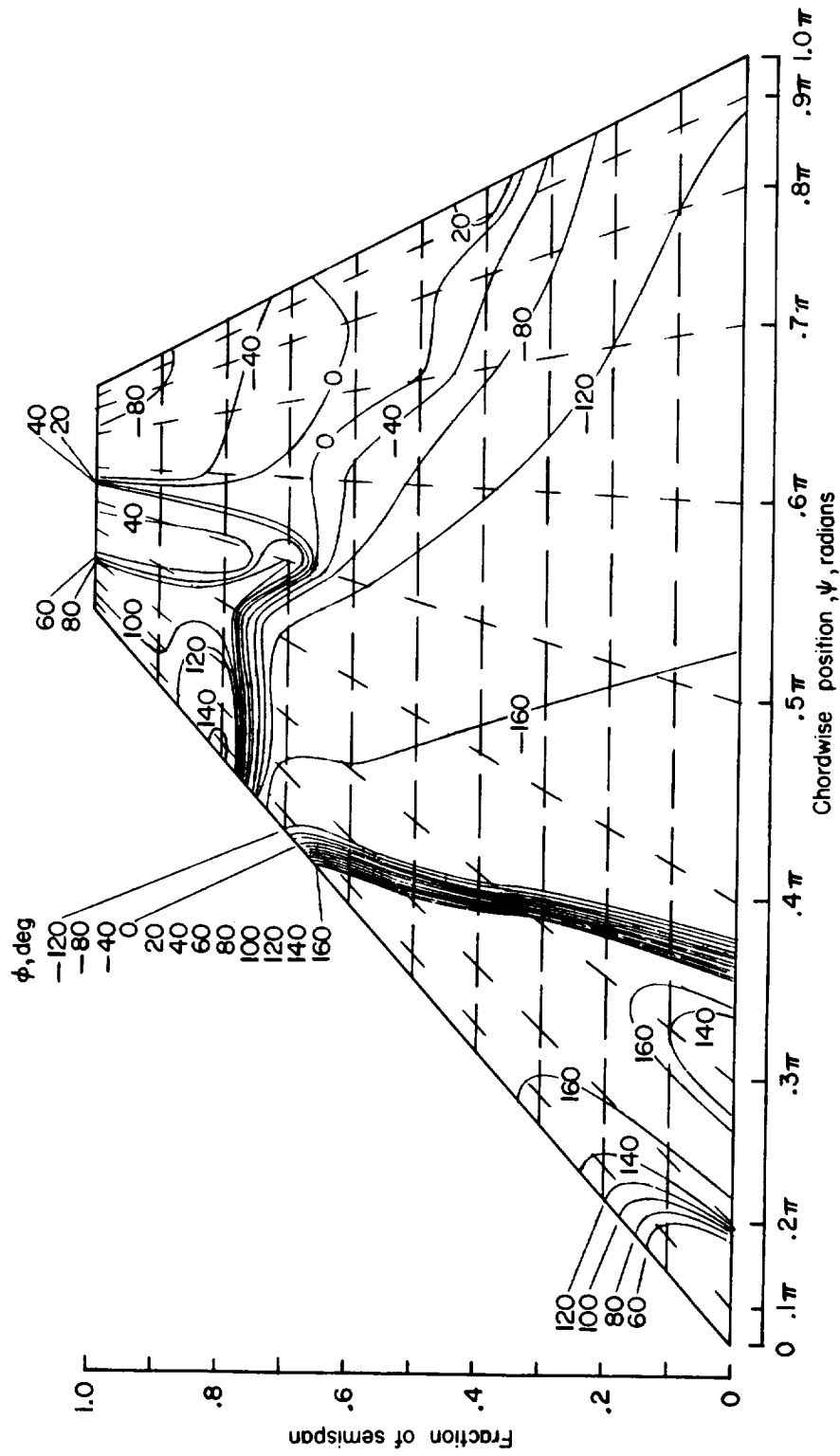
(b)  $M = 0.75$ ;  $k_0 = 0.254$ .

Figure 8.- Continued.



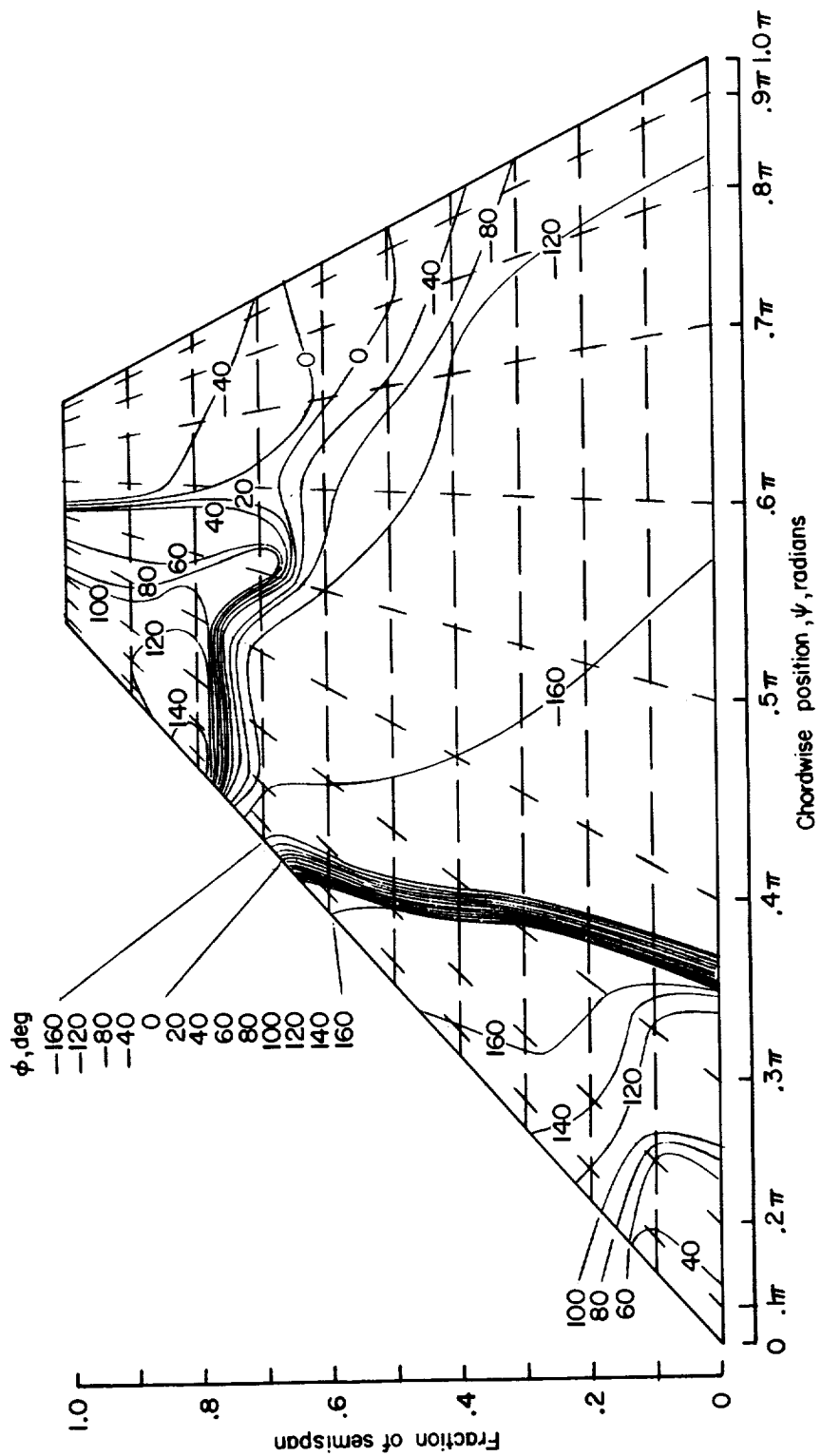
(c)  $M = 0.80$ ;  $k_0 = 0.2525$ .

Figure 8.- Continued.



(a)  $M = 0.85$ ;  $k_0 = 0.248$ .

Figure 8.- Continued.



(e)  $M = 0.90$ ;  $k_0 = 0.245$ .

Figure 8.- Concluded.